First-principle study of the solubility and diffusion of oxygen and boron in γ-TiAl

Enrica Epifano, Gilles Hug

First-principle study of the solubility and diffusion of oxygen and boron in γ–TiAl

E. Epifano and G. Hug[a]

[a]*Laboratoire d'Etudes des Microstructures, CNRS-ONERA, Boite Postale 72, 92322 Châtillon Cedex, France*

Abstract

Solubility and diffusion of boron and oxygen in the γ-TiAl intermetallic compound are herein investigated by first-principle calculations. On the basis of the space group of the γ phase, the accommodation of the light atoms in the various interstitial positions is studied by density functional theory. Diffusion coefficients are also obtained from *ab initio* calculations. Barrier energies for the boron and oxygen diffusion among the different stable interstitial sites are computed using the Nudged Elastic Band method and atomic jumping rates are obtained from the Transitional State Theory. Diffusion coefficients are obtained from the solution of the transport equation in the infinite time limit, using the analytical Multi-State Diffusion method. The methodology here applied is validated by the good agreement between the computed diffusion coefficient of boron and the experimental data available in the literature for this species.

1. Introduction

Titanium aluminides are very promising materials for applications in aerospace, auto-mobile and marine industries, thanks to their relatively low density combined with excellent mechanical properties at high temperatures [1, 2]. Indeed, new TiAl-based alloys are adopted for the last generation turbomachines in airplanes and their use is likely to increase in future engines [3]. In this evolution, the environmental conditions will move to higher temperature and pressure, which will allow improving the efficiency of the engines and hence reducing their environmental impact. However, this entails the need to thoroughly investigate the behaviour of these materials under the new working conditions. Among the properties of interest, the oxidation resistance is essential for such applications.

The Ti-Al system contains essentially three main intermetallic compounds: α_2–Ti_3Al, γ–TiAl and $TiAl_3$ [4]. All these compounds result from an ordering of Al and Ti atoms on a hexagonal compact (*hc*), as Ti_3Al, or face centred cubic (*fcc*) lattice, as TiAl and $TiAl_3$, which stems from a tendency to maximise the Ti-Al pairs. As a consequence of the ordering, γ-TiAl and $TiAl_3$ crystallize under the $P4/mmm$ space group and α_2-Ti_3Al under the $P6_3/mmc$ space group, also referred as $L1_0$, DO_{22} and DO_{19} structures, respectively (see Fig. 1).

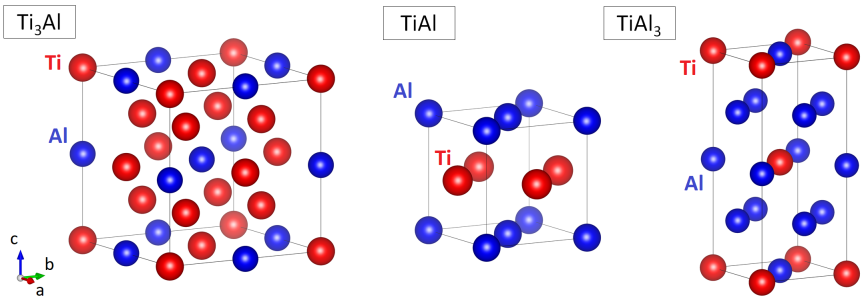

Figure 1: The three intermetallic compounds: (from left to right) α_2-Ti_3Al, γ-TiAl, $TiAl_3$.

$TiAl_3$ has the best oxidation resistance, due to the formation of a dense, passivating scale of alumina with corundum structure (Al_2O_3) [5]. Despite this, $TiAl_3$ is not considered for industrial applications because it is rather brittle.

Ti_3Al and TiAl have the best mechanical properties, but unfortunately these compounds have lower oxidation resistance. Indeed, the increase of the titanium content induces a decrease of the aluminium activity and this leads to the competitive formation of alumina and titanium oxides (TiO and TiO_2) [6, 7, 8]. Several studies have been dedicated to understand and improve the oxidation behaviour of these compounds [9, 10, 11, 12, 13, 14, 15, 16, 17]. Becker *et al.* [6] have shown that, in the 1000-1270 K temperature range, the oxidation of γ-TiAl proceeds with the formation, at first, of a TiO_2 scale and, in a second time, of a passivating Al_2O_3 layer between TiO_2 and the metal. The observed rates indicate that the oxidation is mainly dominated by bulk diffusion. In particular, Maleka [18] has recently shown that the oxidation process takes place as a result of the outward diffusion of titanium and aluminium, as well as the inward diffusion of oxygen. Therefore, for a complete understanding of the oxidation mechanisms, the knowledge of the diffusion coefficients of all the species involved in the process is necessary. While various measurements of the Al and Ti self-diffusion coefficients in Ti-Al intermetallics are reported in the literature [19, 20, 21], few data exist for the oxygen diffusion coefficients in these compounds. Koizumi *et al.* [22] measured the diffusion coefficients of oxygen in Ti_3Al single crystals, for temperatures between 723 and 1073 K, using ion implantation and Auger electron spectroscopy. Bakulin *et al.* [23] performed a theoretical study of the same system, based on DFT calculations to find the energy barriers of oxygen diffusion between interstitial sites, and they obtained a fair agreement with the experimental data from Koizumi *et al.* [22]. To the best of our knowledge, no experimental data are available for the diffusion coefficients of oxygen in γ-TiAl. This is likely due to the extreme difficulty of the experiments for this system: in addition to all the usual problems related with such complex measurements (need for samples with high purity, availability of radio-tracers etc.), the solubility of oxygen in γ-TiAl ($\lesssim$ 3 at.%) is very low [24] and hence the precipitation of rutile and alumina easily occurs (contrary to Ti_3Al, where oxygen solubility is around 13 at.% [25]). Therefore, in order to realize such measurements, it would be necessary to hinder the precipitation of oxides by precisely controlling very low concentration of oxygen, at high temperature, which is clearly very complicated considering its gaseous state and its natural presence in the atmosphere.

Nevertheless, theoretical works have addressed the atomic-scale behaviour of oxygen in γ-TiAl. Most of these studies have focused on the mechanisms of oxygen adsorption on the γ-TiAl surfaces and its diffusion in the subsurface layers [26, 27, 28, 29]. Zhao *et al.* [30] used DFT to compute the barrier energies for the oxygen diffusion in bulk γ-TiAl and Nb-doped γ-TiAl, but they did not provide diffusion coefficients. Kulkova *et al.* extended the investigation and provided computed values for the diffusion coefficients of oxygen in bulk γ-TiAl [31]. These authors adopted the same computation scheme previously adopted by Bakulin *et al.* for Ti_3Al [23]: barrier energies ΔE were obtained by DFT calculations and jump frequencies ν^* were estimated as $\sqrt{\Delta E/(2md^2)}$, with m being the oxygen mass and d the path length. The diffusion coefficients were then obtained by extending the theory proposed by Bertin *et al.* [32] for the oxygen diffusion in α-Ti. This consists in enumerating all the possible diffusion paths, considering both direct jumps and intermediate steps, calculating their probability and then sum all the corresponding diffusion coefficients. Although this approach is valid, it is affect by a high degree of approximation (jump frequencies) and the need to enumerate the possible paths can easily lead to mistakes. Recently, a different approach has been developed to obtain diffusion coefficients from *ab initio* methods. This combines DFT calculations and Transitional State Theory [33] with analytical [34] or Monte Carlo [35] solutions of the diffusion equations. Computations based on this scheme have been successfully applied to obtain the diffusion coefficients of light atoms in monoatomic metals, such as aluminum [36], titanium [37, 38, 35] and nickel [39, 36]. Moreover, the same computation methodology has been recently applied to study the hydrogen diffusion in γ-TiAl [40]. This more rigorous method is here applied to compute the diffusion coefficients of oxygen in γ-TiAl and the results are compared to the previous values from Kulkova *et al* [31].

Next to oxygen, calculations are also performed for boron diffusion. This element is often used as dopant for Ti_3Al-TiAl based alloys, in order to improve the mechanical properties [41, 42, 43, 44, 45, 46, 47]. Boron has a very low solubility in these phases [48, 45, 49] and its addition leads to the precipitation of boride particles, especially TiB_2, which induces a grain refinement, resulting in an improvement of ductility and deformability in the alloys.
Tracer diffusion of boron in polycrystalline γ-TiAl was measured by Divinski *et al.* [50], using secondary ion mass spectroscopy. Since boron and oxygen are both light atoms that diffuse in metallic lattices through interstitial sites, the comparison of the computation results with the data from Divinski *et al.* [50] will allow validating our methodology. Moreover, the computations will allow a better understanding of the atomic-scale processes involved in the boron diffusion and investigating possible anisotropic behaviours, not shown by the available experimental data.

2. Methods

2.1. Theoretical framework

In thermally activated processes, such as the diffusion of an interstitial impurity atom in a crystal, the Boltzmann factor makes certain that the process proceeds via the Minimum Energy Path (MEP). Various methods have been proposed to solve the problem of finding the MEP for an arrangement of atoms from one stable configuration to another [34]. In this work, we used the Nudged Elastic Band (NEB) and the Climbing Image (CI-NEB) methods, as implemented in the VASP code [51, 52], in order to identify the MEP and the relative saddle point, corresponding to the potential energy maximum.

Once determined the MEP and the relative activation energy barrier ΔE, the Transitional State Theory formulated by Eyring [33] was used to study the diffusion of oxygen atoms. According do this theory, the jump rate ν, which quantifies the probability of an atom to leave its site, is given by the following Arrhenius equation:

$$\nu = \nu^* e^{-\Delta E/k_b T} = \frac{k_B T}{h} \frac{Z_{ts}}{Z_{ie}} e^{-\Delta E/k_b T} \tag{1}$$

where k_B and h are respectively the Boltzmann and the Planck constant, T is the temperature, Z_{ts} and Z_{ie} are the vibrational partition functions for the transition state and the initial equilibrium point, respectively. The ν^* pre-factor is usually referred as an *attempt frequency*. Z functions are related to the Helmholtz free energy F and they are generally expressed as [53]:

$$F = -k_B T lnZ = k_B T \sum_{\mathbf{q}_i}^{N} ln\left[2sinh\left(-\frac{hw_{\mathbf{q}_i}}{2k_B T}\right)\right] \tag{2}$$

where $w_{\mathbf{q}_i}$ is the frequency of the i mode in the $\mathbf{q}$ point and the sum is over all the modes. The phonon calculations to obtain these frequencies need to include all the atoms of the system, and not only the diffusing one [39]. Therefore, this approach takes into account the full coupling of the vibrational modes between the diffusing atom and the lattice.

Eq. 2 is generally valid, regardless of the order of the transition state, i.e. whether there is only one imaginary mode (first order) or several. In the high-temperature limit and in presence of only first-order transition states, the vibrational partition functions are expressed in terms of the N normal modes of the system in the equilibrium state and the $N-1$ modes (excluded the imaginary one) at the saddle point [54, 36] and the pre-factor becomes:

$$\nu^* = \frac{1}{2\pi} \frac{\prod_{i=1}^{N} w_i^{ie}}{\prod_{i=1}^{N-1} w_i^{s}} \tag{3}$$

where w_i^s and w_i^{ie} are the frequencies computed at the center of the Brillouin zone, for the saddle and the equilibrium points, respectively. The latter equation is not valid if higher order transition states (more than one imaginary mode) are considered, because ν^* must be a frequency. In this work, the general expression of Eq. 2 has been adopted.

Once the jumping rate ν is obtained, following Wert and Zener [55], for simple single-state diffusion, the diffusion coefficient D is:

$$D = n\beta d^2 \nu \tag{4}$$

where n is the number of nearest-neighbour stable sites for the diffusing atom, β is the probability that a jump to a nearest-neighbour site leads forward in the diffusion direction and d is the projection of the jump length onto the direction of diffusion. Again, this equation is valid only for single-state diffusion, i.e. if there is only one possible path. For more complex diffusion process, where an atom can randomly migrate among several internal states with different jumping rates, the analytical Multi-State Diffusion method [34, 56] can be applied to find the diffusion coefficients [36, 35, 37]. The first step is identifying all the N different kinds of jumps among the various sites occupied by the diffusing atom. Each jump is characterized by a displacement and a waiting time distribution function. Then, the NxN Laplace transform matrix of the waiting-time function, $\underline{\psi}(u)$, and the NxN Fourier transform matrix of the displacements, $\underline{p}(\overrightarrow{k})$, have to be built. From these, the propagator matrix $\underline{R}(\overrightarrow{k}, u)$ is obtained as the difference between the identity matrix and the Hadamard product of the previously defined matrices:

$$\underline{R}(\overrightarrow{k}, u) = [\underline{I} - \underline{p}(\overrightarrow{k}) \odot \underline{\psi}(u)]. \tag{5}$$

The diffusion variance $\sigma_r^2(t)$ along a general direction r can be obtained as:

$$\sigma_r^2(t) = \lim_{\vec{k}\to 0} t \frac{1}{\Delta_0} \frac{\partial^2 \Delta}{\partial k_r^2}\bigg|_{u\to 0} \tag{6}$$

where Δ is the determinant of $\underline{R}$ and Δ_0 is

$$\Delta_0 = \lim_{u\to 0} \frac{\Delta(\vec{k}, u)}{u} \tag{7}$$

Finally, the diffusion coefficient along the r direction is obtained as:

$$D_r = \frac{\sigma_r^2(t)}{2t}. \tag{8}$$

2.2. *Light atom insertion*

The $L1_0$-TiAl intermetallic belongs to the tetragonal $P4/m\,mm$ space group (n. 123), with aluminium and titanium occupying the $1d$ and $1a$ Wyckoff positions, respectively. Geometrically, it can be seen as build from two types of structural units, formed by octahedra. The octahedron plays a special role in the close packed structures. It has cubic point symmetry and a packing of octahedra can fill the space of both the fcc or the hc lattices. When a cluster of six identical atoms occupy the vertices of a regular octahedron, one obtains a cluster with cubic point symmetry. The γ–TiAl compound contains an equal number of two different octahedra: one formed by 4 Ti and 2 Al and the other by 4 Al and 2 Ti (see Fig. 2). The centres of these octahedra correspond to the *1c* and *1b* Wyckoff positions, respectively. In the following, the notation $[Ti_4Al_2]$ and $[Ti_2Al_4]$ is used to distinguish these two interstitial sites by the kind of atoms that occupy the six vertices of the octahedra.

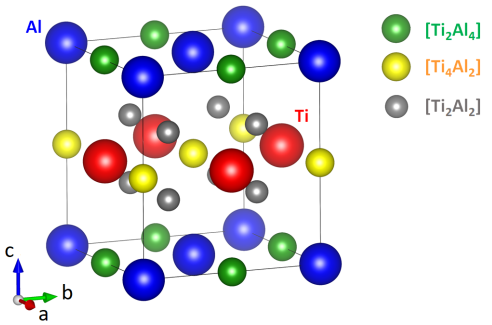

Figure 2: γ-TiAl with Ti atoms in red and Al in blue. Octahedra and tetrahedra interstitial sites are shown: $[Ti_2Al_4]$ in green, $[Ti_4Al_2]$ in yellow and $[Ti_2Al_2]$ in grey.

In metals and metallic alloys, atoms of oxygen and boron, as well as other light elements like carbon and nitrogen, in low concentration, are likely to dissolve in the cavities formed by the structure of the crystal. In the close-packed metals with face centred cubic (fcc) or hexagonal compact (hc) lattice two types of cavities exist: either the tetrahedra or the octahedra [36]. In γ-TiAl, in addition to the two octahedra already mentioned, tetrahedral cavities formed by 2 Ti and 2 Al atoms are also present (see Fig. 2), herein named $[Ti_2Al_2]$. In general, tetrahedra are convenient for the smaller atoms like hydrogen, while they are too small for the boron, carbon, nitrogen and oxygen atoms. These atoms are more easily hosted in the octahedral cavities. An important point is that the cubic point symmetry of the octahedron is compatible with the p orbitals of light elements. The electronic structures of boron, carbon, nitrogen and oxygen are $2s^22p^1$, $2s^22p^2$, $2s^22p^3$ and $2s^22p^4$, respectively. When such atoms are inserted in an octahedron cavity, the p_x, p_y and p_z orbitals of the valence electrons can point toward the vertices of the octahedron. If a transition metal (TM) is located at the vertices, hybrids $3d$ orbitals of the TM and the $2p$ orbitals of the light element can be easily formed. Indeed, the crystallographic structures of TiC and TiN are NaCl-type, that is two fcc lattices, one for Ti and

one for C or N, which are shifted by [1/2, 1/2, 1/2]. In these compounds, the C, N atoms are located in Ti octahedra. In some respect TiO shares the same structure although it is only stable in under-stoichiometric composition (i. e. TiO_x, with $x < 1$) in which an ordering of the vacancies on the oxygen sub-lattice can occur [57]. However, the presence of suitable cavities in such a geometric analysis is not sufficient to ensure that an element like oxygen can be dissolved in the metallic matrix. It is necessary also that the chemical composition is compatible with the formation of bonds. For this reason, it is necessary to look at all the kind of possible insertion sites.

2.3. Computational details

All electronic structure calculations were performed with the VASP code [51, 52]. Self-consistent Kohn-Sham equations were solved using the projector augmented wave (PAW) pseudopotentials [58]. The Perdew-Burke-Ernzerhof (GGA-PBE) exchange and correlation functionals were used [59]. Based on convergence tests, the plane-wave cutoff energy was set at 500 eV and 1000 k-points were used in the conventional pseudo-cubic unit cell of γ-TiAl (i.e. the 4 atoms cell). The k-point density was kept roughly constant for the other structures and supercell calculations. Such parameters provides a numerical accuracy in the range of 10^{-6} eV. 3 x 3 x 3 super-cells were used to study the accommodation of oxygen and boron defects, as well as for NEB calculations. The structural optimizations were performed by fully relaxing atomic positions and lattice parameters (shapes and volumes). The NEB and CI-NEB calculations were instead performed on cells with fixed dimensions, by relaxing only the atomic positions. The number of used images was 5 or 7, depending on the length of the considered path. The NEB computations were carried on until reaching a convergence of 10^{-4} eV on the image with maximum energy. The duration of these calculations is in the order of 10^4 cpu hours. Vibrational properties and interatomic force constants were obtained by a finite displacement method (FDM), using the *phonopy* code [60]. Phonon calculations were performed using 3x3x3 supercells, with the same energy cutoff, k-points and energy convergence criterion used for the other calculations. Besides, an additional convergence criterion of 10^{-7} eV/Å was used for the forces.

3. Results

3.1. Pure elements and defect-free structures

The equilibrium lattice parameters obtained for the pure elements are shown in Table 1. They are in general good agreement with the data in the literature. In the same table, the total energies are reported as reference values for the chemical potential of the pure elements.

Table 1: Reference total energies (E_{tot}) of the elements and equilibrium lattice parameters. The italic numbers correspond to the known experimental values [61]. For oxygen, the a value refers to the inter-atomic distance in the O_2 molecule.

Element	structure	E_{tot} (eV.atom^{-1})	a (Å)	c (Å)
Ti	hc	-7.890	2.95 (*2.95*)	4.61 (*4.685*)
Al	fcc	-3.747	4.04 (*4.049*)	-
B	$R\bar{3}m$	-6.680	10.92 (*10.95*)	23.73 (*23.90*)
O_2	molecule	-4.474	1.23 (*1.21*)	-

The conventional cell of γ-TiAl, formed of 4 atoms, was optimized with respect to volume and c/a ratio. The lattice parameters after optimization (see Table 2) are in very good agreement with the experimental values [61] and with previous DFT studies [29]. The enthalpy of formation of the stoichiometric γ-TiAl compound is computed as:

$$H_{form} = \frac{1}{N}\left(E_{tot} - \sum_{i}^{N} \mu_i\right) \tag{9}$$

where E_{tot} is the total energy for the considered cell of N atoms and the summation includes the chemical potential of all the atomic species in their stable pure form (provided in Table 1). The obtained value, also reported in Table 2, is in very good agreement with both experimental [62] and theoretical [29] data from literature.

Table 2: Calculated lattice parameters, total energy and formation enthalpies of γ-TiAl, compared with previous DFT studies and experimental data. The experimental lattice parameters are from [61] and the enthalpy of formation from [62].

	a (Å)	c (Å)	E_{tot} (eV/uc)	H_{form} (eV/atom)
DFT-this work	3.991	4.073	-24.729	-0.409
Experiment	4.000	4.075		-0.39 ± 0.02
DFT [29]	3.989	4.068		-0.415

3.2. Static relaxation with interstitials

Three main interstitial sites are considered for the accommodation of boron and oxygen in γ-TiAl (see Fig. 2): two octahedra and one tetrahedron. One oxygen atom and one boron atom have been (separately) inserted in the centres of these sites. For this purpose $3 \times 3 \times 3$ supercells were used. All the lattice parameters and atomic positions have been relaxed to find the minimum energy configuration. The obtained total energies and enthalpies of formation (computed using Eq. 9) are shown in table 3. In the same table, the formation energies of the defects are also reported. These represent the energies required to insert a solute atom in a perfect γ-TiAl lattice and their general definition is [63] :

$$E_{def}\left[\mathrm{I}_p^q\right] = E_{\mathrm{tot}}\left[\mathrm{I}_p^q\right] - E_{\mathrm{tot}}\left[\mathrm{bulk}\right] - \sum_i n_i\mu_i + qE_F + E_{\mathrm{corr}} \tag{10}$$

where $E_{\mathrm{tot}}\left[\mathrm{I}_p^q\right]$ is the total energy, derived from a supercell calculation containing the interstitial defect I, at site p, and $E_{\mathrm{tot}}\left[\mathrm{bulk}\right]$ is the total energy for the perfect crystal, obtained using an equivalent supercell. The integer n_i indicates the number of atoms with chemical potential μ_i that have been added, which is limited to one in our case. The variable q refers to a possible charge of the interstitial atom and E_F is the Fermi energy. E_{corr}, finally, is a correction term that accounts for finite **k**-point sampling and for elastic and/or electrostatic interactions between supercells [63]. Some approximations were here introduced in the calculation of the formation energy of defects. First, defects were considered as uncharged. In a metallic compound such as γ-TiAl, it can be assumed that an efficient screening takes place and, in first approximation, the qE_F term can be neglected. Second, the E_{corr} has not been taken into account; however, an estimation of the supercell size effect is reported in Appendix A. Finally, in the general formalism, chemical potentials are regarded as variables [64], whose bounds are set by the existence of secondary phases (in this case, oxides and borides). Herein, the chemical potentials were set to the values of pure elements (table 1). This approximation is adopted since the aim of this work is not quantifying the solubility of O and B in γ-TiAl (data exist in the literature), but determining in which interstitial sites these atoms can be accommodated. In summary, the energy of formation has been computed with the approximated formula:

$$E_{def}\left[\mathrm{I}_p\right] = E_{\mathrm{tot}}\left[\mathrm{I}_p\right] - E_{\mathrm{tot}}\left[\mathrm{bulk}\right] - \mu_i. \tag{11}$$

The same approximation was used by Kulkova *et al.* [31], who studied the diffusion of oxygen in γ-TiAl. The values for the octahedral sites agree quite well with this previous work from Kulkova *et al.*: $E_{def} = -3.205$ eV (this work) and -3.07 eV [31] for $[Ti_2Al_4]$; $E_{def} = -4.223$ eV (this work) and -4.02 eV [31] for $[Ti_4Al_2]$. On the contrary, the formation energy of the tetrahedral site provided by Kulkova (-3.17 eV) is in clear contrast with our positive value of +1.350 eV. Such big difference cannot be simply due to numerical approximations, especially considering the agreement for the other sites, and its origin remains unclear. However, the similarity of the calculations for both oxygen and boron gives confidence to the data of this work. Besides, as already mentioned in section 2.2, the tetrahedral interstitial sites are generally preferred by very light atoms as hydrogen [40], but they are too small for being energetically stable for atoms such as oxygen [65] and boron. The calculations of this work confirm this trend: the formation energy of O and B defects in tetrahedra are higher than 1 eV (1.350 and 1.678 eV, respectively). Indeed, the computed values shown in Tab. 3 indicate a clear preference for the octahedral sites, rather than for the tetrahedra, for both oxygen and boron. This indicates that these atoms have a low probability to be found in the tetrahedra and hence their contribution to the diffusion is secondary in comparison to the octahedral sites. For this reason, in first approximation, only the latter have been considered in the rest of the work.

Table 3: Formation enthalpies H_{form} and defect energies E_{def} for B or O insertion in γ-TiAl. E_{tot} refers to the total energy of the $3\times3\times3$ supercell (sc) with one interstital atom.

Atom	Site	E_{tot} (eV/sc)	H_{form} (eV/atom)	E_{def} (eV/atom)
B	$[Ti_2Al_4]$	-673.591	-0.397	0.768
	$[Ti_4Al_2]$	-674.673	-0.407	-0.313
	$[Ti_2Al_2]$	-672.682	-0.389	1.678
O	$[Ti_2Al_4]$	-675.362	-0.390	-3.205
	$[Ti_4Al_2]$	-676.380	-0.399	-4.223
	$[Ti_2Al_2]$	-670.807	-0.348	1.350
	α	-676.020	-0.396	-3.863
	β	-676.547	-0.401	-4.390

Between the two octahedral sites, for both the elements, the center of the $[Ti_4Al_2]$ octahedron is the stablest position. The oxygen preference for the Ti-rich site is in agreement with several previous works [26, 27, 28, 29, 31].

It is worth mentioning that, after the relaxation of the atomic positions, both oxygen and boron remained in their initial position, i.e. in the exact centres of the octahedra. However, it should be noted that all forces on these atoms vanish "by symmetry" during the calculation. For this reason, the dynamical stability of the relaxed configurations has been studied by calculating the phonon band structure, using the finite difference method as described in section 2. The partial vibration density of states of boron and oxygen, in these configurations, are shown in Fig. 3.a-b and Fig. 4.a-b, respectively. The red curve corresponds to the projection in the basal plane, while the blue curve is the projection onto the c axis direction.

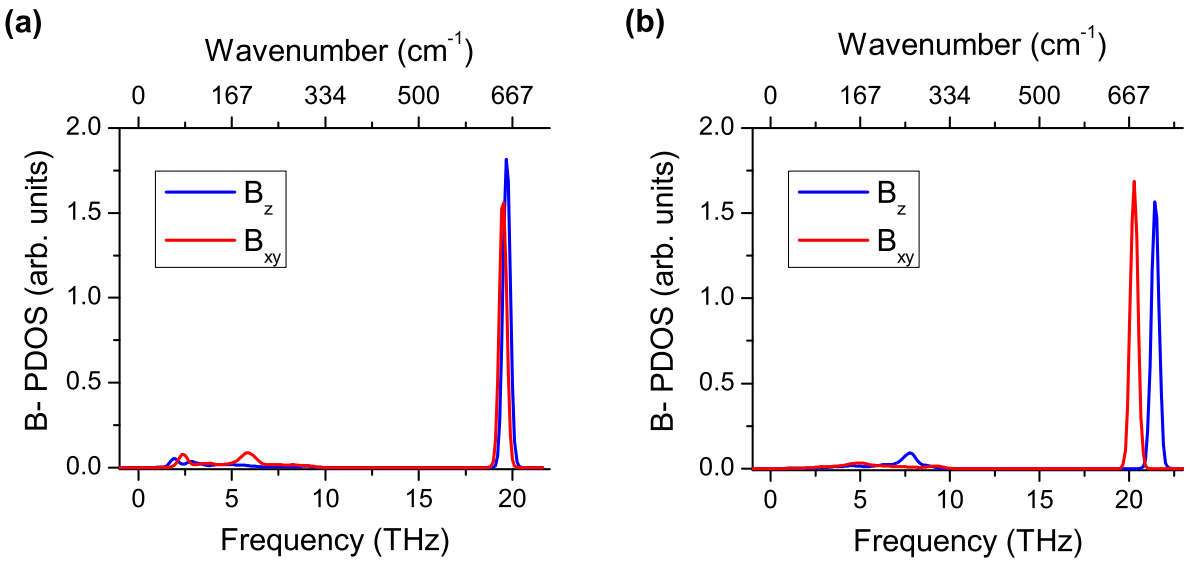

Figure 3: Partial vibrational density of states (PVDOS) of a solute boron atom in the γ-TiAl matrix. Boron located at the center of $[Ti_2Al_4]$ (a) and $[Ti_4Al_2]$ (b) octahedra. The red and blue curves correspond to vibrations in the basal plane and along the c axis, respectively.

For boron, only positive frequencies are observed, indicating that it is stable in both the octahedral sites. For both the positions, high-frequency vibration modes are observed around 20 THz, both in the basal plane and the

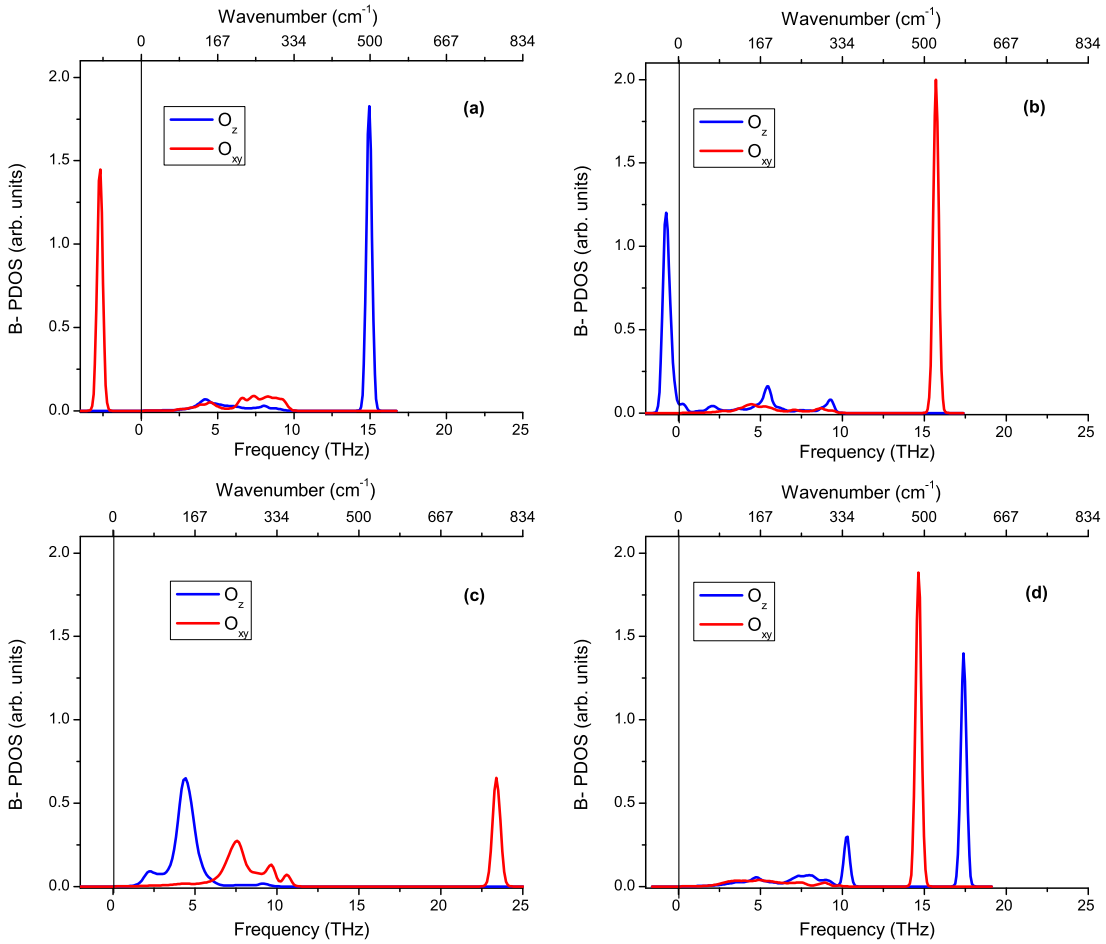

Figure 4: Partial vibrational density of states (PVDOS) of a solute oxygen atom in the γ-TiAl matrix. Oxygen located at the center of a $[Ti_2Al_4]$ octahedron before (a) and after full relaxation (c). Oxygen atom at the center of a $[Ti_4Al_2]$ octahedron before (b) and after full relaxation (d). The red and blue curves correspond to vibrations in the basal plane and along the c axis, respectively.

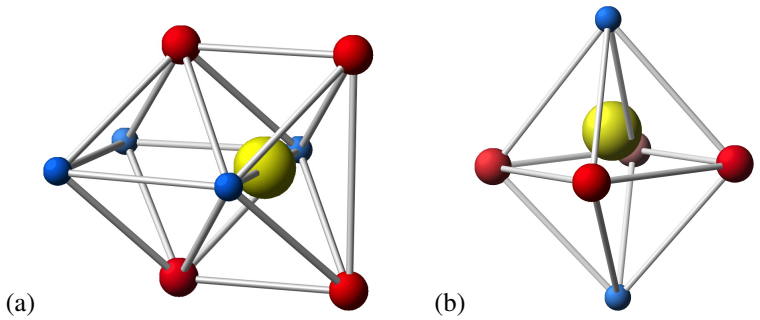

Figure 5: Final positions of the oxygen atom (yellow) after relaxation. The aluminium and titanium atoms are represented in blue and red, respectively. In (a) the oxygen atom originally at the center of the $[Ti_2Al_4]$ octahedron has moved to the edge of the octahedron, between two aluminium atoms. In (b) the oxygen atom, originally at the center of the $[Ti_4Al_2]$ octahedron, has moved up to the center of the square pyramid.

perpendicular direction. These indicate that boron forms strong and rigid bonds with both Al and Ti atoms.

Contrary to the boron case, a significant *negative* frequency appears in the vibrational band structure of oxygen in both octahedral sites. This is a sign of the presence of an imaginary mode related to a mechanical instability of the structure. From the partial density of states shown in Fig. 4.a and Fig. 4.b, it is clear that the oxygen is unstable in the basal plane, for the $[Ti_2Al_4]$ octahedron (Fig. 4.a), and in the z direction, for the $[Ti_4Al_2]$ octahedron (Fig. 4.c).

Starting from the relaxed structure, the oxygen atom was displaced from its high symmetry position by 0.02 Å in the three directions of space and the relaxation process was restarted. For $[Ti_2Al_4]$, after the optimization, the oxygen atom was back in the initial basal plane, i.e. the initial displacement of 0.02 Å in the z direction was cancelled. However, the relaxed position is not in the centre, but in the edge of the initial octahedron. The resulting configuration corresponds to the 2*e* Wyckoff position and it can be seen as the center of a distorted octahedron, with two aluminium and four titanium atoms at the vertices. The first nearest neighbours of the oxygen are two aluminium atoms, at a distance of $d_{\text{O-Al}} = 1.80$ Å, a value which is very close to the O–Al distance in α-Al_2O_3 alumina. The second nearest neighbours consist of four titanium atoms, at a distance of $d_{\text{O-Ti}} = 2.33$ Å, consistently with the corresponding distance in the TiO cubic compound. The configuration around oxygen is schematized in Figure 5a. This defect position will be labelled "α" in the following. The same procedure was applied in the case of the $[Ti_4Al_2]$ octahedron. The optimized position of the oxygen atom was found to be at the center of one of the two square pyramids forming the initial octahedron. It means that the equilibrium position is only shifted by roughly 0.5 Å in the z direction, with no displacement along the two other axis (Figure 5b). The distance from the oxygen atom to the aluminium atom at the top of the pyramid is 1.83 Å and the distances from oxygen to the four titanium atoms is 2.09 Å. Here again, the oxygen to metal atom distances are consistent with the observed distances in oxides. This configuration will be labelled "β" herein.

The VDOS of oxygen in the two fully relaxed configurations (Fig. 4.c and 4.d) show that the imaginary frequencies have disappeared. Interestingly, in the case of the relaxation from $[Ti_2Al_4]$ toward α, the VDOS has changed to a much more dispersed picture. The previous negative frequency in the basal plane has separated into one sharply peaked resonance, at very high frequency (24 THz), and a "group of resonances", in the range of 6 to 11 THz. The former corresponds obviously to a vibration in the direction of the two Al first neighbours, which are close and expected to be strong and rigid bonds. In the perpendicular direction, the oxygen atom has no close neighbours, which allows a relatively easy motion consistently with the low frequency observed in the VDOS. Along the z direction, a reversed behaviour is observed. In the non-relaxed configuration, the oxygen atoms would vibrate in the z direction towards a Ti atom, which can be assume to be a difficult process. Consistently, in Fig.4.a, a high frequency (15 THz) peaked mode shows up in the VDOS. After relaxation, the motion of the oxygen atom along z points in between two titanium atoms and perpendicular to the Al-O bonds. Therefore, the Al-O bonds are not strongly solicited and the O-Ti only moderately. This results in a strong dispersion of the vibration mode along z: the frequency is shifted to 5 THz or less and strongly dispersed.

In the VDOS of the relaxed position β (Fig. 4.d), similar features show up. The vibration in the basal plane is red-shifted from slightly above to slightly below 15 THz. This is due to the fact that the Ti-O bonds are slightly unaligned when the oxygen atom moves in a $\{x, y\}$ plane located "above" the plane of the titanium first neighbours. In

the z direction, the peak at negative frequency in Fig.4.d is shifted to positive frequency and split in two main modes at 10 and 18 THz. Therefore, in the z direction the oxygen atom has two vibrational modes. This is consistent with a "hard" one, at 18 THz, connected with the aluminium first neighbour and a softer one, at 10 THz, connected with the other aluminium and titanium atoms (second & third neighbour).

After, the full relaxation of the supercell, the site energy difference is lowered, i.e. $E^{\alpha}_{\text{tot}} - E^{\beta}_{\text{tot}} = 0.527$ eV, while the ΔE between the centres of the octahdra was 1.02 eV (in favour of $[Ti_4Al_2]$). Such difference is due to the fact that the symmetry breaking is more effective for the α site, rather than the β.

In summary, combining the information obtained from formation energies and dynamic stability, it is possible to choose the sites to be considered for the diffusion. For oxygen, only the α and β sites are taken into account, since the centres of the octahedra are not dynamically stables. For boron, both $[Ti_4Al_2]$ and $[Ti_2Al_4]$ are considered.

3.3. Energy barriers

In order to evaluate the diffusion processes of solute atoms in γ-TiAl, one has to consider the energy barrier to overcome when these atoms move from one stable position to another. The motion from one stable site to a neighbouring stable site constitutes a single step in the diffusion of a solute atom. Here, several possible steps, i.e. initial/final positions, have been considered and, for each of these, NEB calculations have been performed, in order to identify the highest energy point and the relative barrier energy of each step.

The results of the NEB calculations for the diffusion of oxygen in γ-TiAl are summarized in Table 4. Several paths among the α and β sites have been considered.

$\alpha \rightarrow \alpha$. First, the diffusion of oxygen between two α sites belonging to the same basal plane of Al atoms is considered. Such a plane is shown in Figure 6, in the form of an energy map. This latter was obtained by performing several DFT calculations, in which all the atomic positions were relaxed, except that of oxygen, for which the x/a and y/b coordinates were fixed in the various positions of the plane. The lowest energy points, the α sites, are the blue regions in Figure 6.

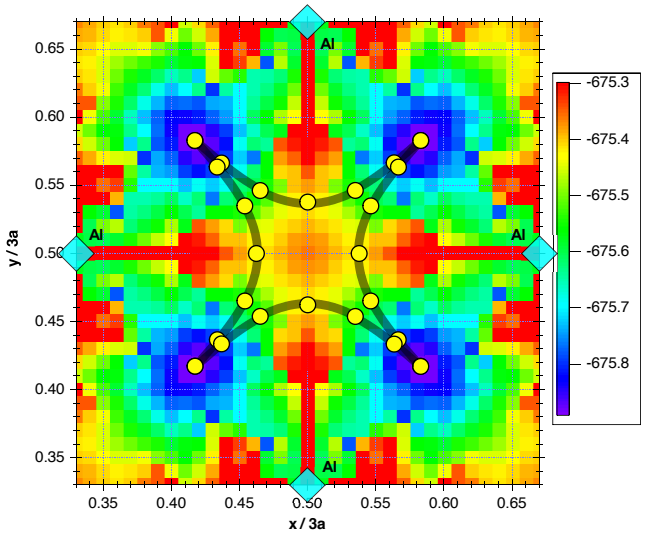

Figure 6: Energy map of the basal plane containing the α defects (blue region) and NEB results (yellow points connected by a black curve).

Two different paths are evaluated: the shortest one, named P_1, corresponds to a movement along the a (or equivalently b) axis, with a distance of ~2 Å; the second path, named P_2, corresponds to the jumping along the diagonal of the plane, through the centre of the octahedron, with a distance of ~2.83 Å. For P_1, a simple linear interpolation between α_0 and α_1 was used as input trajectory for the NEB calculations. The NEB result is shown by the yellow dots in Figure 6. The MEP lies in the basal plane (c = constant), but it differs from a straight line: the atom moves toward

the centre of the octahedron, without reaching it, on a curved trajectory, avoiding the highest energy points. It must be mentioned that attempts to move the path out of the basal plane (c ≠ constant) were made, but the calculations re-converged on the shown MEP. The centre of this path coincides with the highest energy point, with an energy barrier of 0.758 eV.

For the P_2 path, as in the previous case, a linear interpolation between the initial and final sites was used as input trajectory for the NEB calculations, corresponding to a movement along the (a/2, a/2, 0) direction. The NEB results show that the P_2 path is not energetically favoured, but it is divided into two-steps: the oxygen walks twice the MEP previously found, avoiding the center of the octahedron.

The NEB results obtained for the $\alpha \rightarrow \alpha$ diffusion are consistent with the energy map obtained from the static calculations. Indeed, the highest energy points, that are the centre of the octahedron and the sites close to the aluminium atoms on the basal plane, are systematically avoided by the MEP.

$\beta \rightarrow \beta$**.** The simplest path corresponds to the jump of oxygen between two β sites inside the same octahedron, one above the center (as in Figure 5-b) and the other below it. The NEB showed that the MEP basically corresponds to a straight linear trajectory passing for the centre of the octahedron. The latter is the saddle point of this path and the obtained energy barrier is equal to 0.218 eV.

Table 4: Energy barriers of the different paths considered in this study for the oxygen diffusion in γ-TiAl.

Path name	start	end	vector	energy barrier (eV)
P_1	α	α	$(0, a/2, 0)$	0.598
P_2	α	α	$(a/2, a/2, 0)$	= 2·P_1
P_3	β	β	$(0, 0, c/2)$	0.218
P_4	β	α	$(a/4, a/4, c/2)$	1.205
-P_4	α	β	$(a/4, b/4, c/2)$	0.658

More complex and longer trajectories between β sites belonging to different octahedra were also considered, as those represented in Figure 7. The NEB showed that all these paths correspond to two-steps, where the oxygen firstly equilibrate in the α site and then it jumps to the closest β. Hence, the $\alpha \leftrightarrows \beta$ jump is the next discussed.

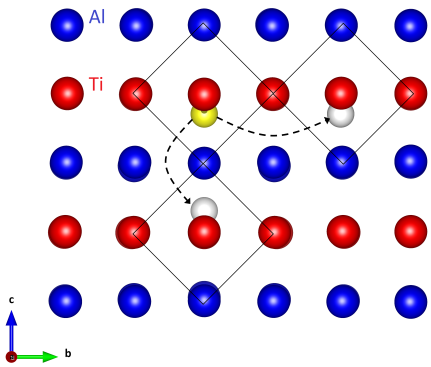

Figure 7: Hypothetical β-β paths between different $[Ti_4Al_2]$ octahedra (traced with a black line).

$\beta \leftrightarrows \alpha$**.** The shortest possible distance between an α and a β site is ~2 Å. The path between two nearest-neighbour sites, here named P_4, has been optimized with the NEB method. The result is a MEP with a non-linear trajectory as the one shown in Figure 8, where the intermediate optimized images are represented in light grey and the highest energy point is in green. The energy profile of this path is not symmetric, since the β site is more stable than the α.

The energy barrier for the $\beta \rightarrow \alpha$ jump is 1.208 eV, whereas in the opposite direction it is lowered to 0.661 eV.

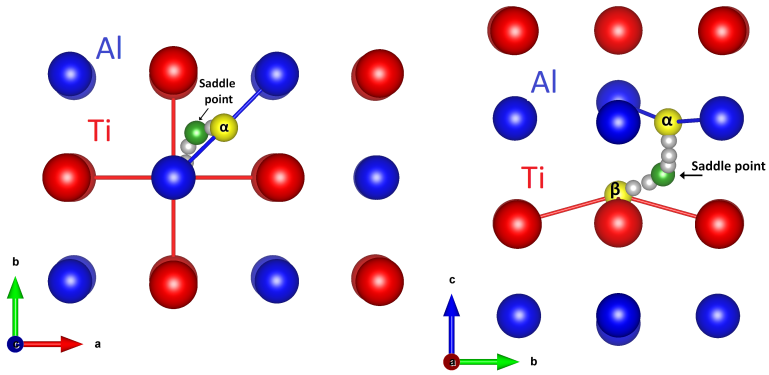

Figure 8: Minimum energy path of oxygen between α and β. Blue = Al, red = Ti, yellow = stable interstitial sites for oxygen, green = saddle point, grey = optimized images from NEB.

Similarly to oxygen, NEB calculations were performed to compute the energy barriers for the jump of boron atoms among the $[Ti_4Al_2]$ and $[Ti_2Al_4]$ sites. The diffusion between two octahedra of the same type, i.e. between two $[Ti_4Al_2]$ or two $[Ti_2Al_4]$, occurs in the basal plane, along the (a/2, a/2, 0) direction, while jumps among different octahedra lead to a diffusion also along the c axis. The results are summarized in Table 5.

Table 5: Energy barriers of the different paths considered in this study for the boron diffusion in γ-TiAl.

Path name	start	end	vector	energy barrier (eV)
Q_1	$[Ti_2Al_4]$	$[Ti_2Al_4]$	$(a/2, a/2, 0)$	0.979
Q_2	$[Ti_4Al_2]$	$[Ti_4Al_2]$	$(a/2, a/2, 0)$	2.996
Q_3	$[Ti_4Al_2]$	$[Ti_2Al_4]$	$(a/2, 0, c/2)$	2.160
$-Q_3$	$[Ti_2Al_4]$	$[Ti_4Al_2]$	$(a/2, 0, c/2)$	1.073

The energy barriers for the diffusion of boron are considerably higher than those of oxygen. In particular, the energy barriers for a boron leaving a $[Ti_4Al_2]$ octahedron are very high: 2.160 eV and 2.996 eV for reaching the neighbour $[Ti_2Al_4]$ and $[Ti_4Al_2]$ sites, respectively. This proves again that the accommodation of boron in the Ti-rich octahedron is energetically very favoured.

3.4. Diffusion coefficients

Phonon calculations were performed for the highest energy point of each diffusion path identified in Table 4, for oxygen, and Table 5, for boron. As expected, at least one imaginary vibration mode was found for each transition state (see Appendix B). The jumping rates were hence computed with Eq. 1-2 (using energy and frequency values at 0 K). The results are shown in Fig. 9-(a) and Fig. 9-(b), for oxygen and boron respectively. The jumping rates of oxygen are around 3-5 orders of magnitude higher than those of boron.

For oxygen, the highest jumping rates ν are exhibited for the P_1 and P_3 paths, respectively between two neighbour α and two neighbour β sites. This is not surprising, since these two jumps are those with the lowest energy barriers: 0.218 eV and 0.598 eV, for $\nu_{\beta-\beta}$ and $\nu_{\alpha-\alpha}$, respectively. However, the β–β P_3 path does not provide a net contribution to the oxygen diffusion in the lattice, because it basically corresponds to a vertical (along z) oscillation inside a $[Ti_4Al_2]$ octahedron. The oxygen atom stays trapped in the same cell and, in order to move forward, it needs to jump toward an α site, for which the relative barrier is high (1.205 eV) and hence the $\beta - \alpha$ jumping rate is very low. On the contrary,

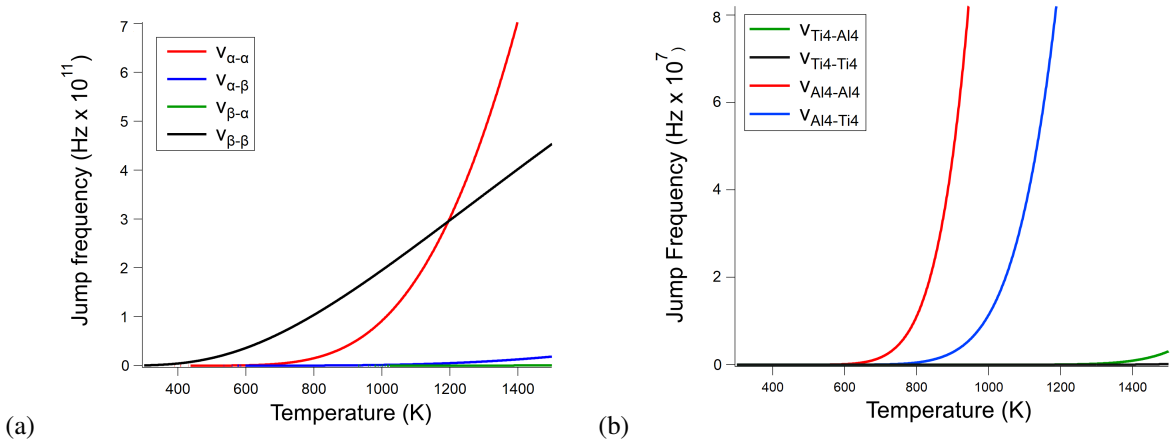

Figure 9: Jumping rates as a function of temperature: (a) oxygen, (b) boron. For simplicity, the octahedral sites are identified with the most abundant element, i.e. *Al*4 indicates the $[Ti_2Al_4]$ octahedron.

the oxygen can diffuse in the basal plane, moving through close α sites. This jumping rate is activated for T $\simeq$ 800 K and it rapidly increases above this temperature. However, an oxygen in an α site has also a non negligible probability to get trapped by the more stable β site, which is represented by the $\nu_{\alpha-\beta}$ jumping rate.

The boron jumping rates, considerably lower than those of oxygen, are activated for temperatures above 600 K, with values $\lesssim 10^8$ Hz. The highest rate is observed for jumps between two neighbour $[Ti_2Al_4]$ sites. Similarly to the $\alpha - \alpha$ path of oxygen, this leads to a diffusion in the basal plane. The same magnitude order is observed for the jumping rate from the $[Ti_2Al_4]$ octahedron to the neighbour $[Ti_4Al_2]$, leading to a diffusion along the c axis. The two jumping rates from the $[Ti_4Al_2]$ are 3 magnitude orders lower than those from the other octahedron. As already mentioned, this is due to the higher stability of this site which leads to very high energy barriers (E > 2 eV). Similarly to the oxygen in the β site, the Ti-rich octahedron in γ-TiAl represents a trap for the boron diffusion.

Considering the possible multiple paths for the diffusion of oxygen and boron in γ-TiAl, the diffusion coefficients were obtained from the multi-state diffusion theory, explained in the methods section 2, using Eq. 5-8. The waiting time and displacement matrices, as well as the diffusion coefficient expressions, as a function of jumping rates and crystallographic parameters, are provided in Appendix C.

The diffusion coefficients as a function of the temperature are shown in Fig.10 and compared to the available experimental data, for boron [50], and to the calculated values from Kulkova [31], for oxygen. A very good agreement between the calculations from this work and the literature data can be observed. In addition, to remark the differences in the magnitude order, the Ti self-diffusion [21] and the hydrogen diffusion coefficients [40] in γ-TiAl are also shown in Fig. 10.

As expected from the symmetry of the lattice, for both oxygen and boron, the diffusion coefficients in the basal plane, D_x and D_y, are equal, whereas a different expression is obtained for the z direction. For both the solute species, the diffusion in the xy plane is faster than along z. The anisotropy is more accentuated for oxygen than boron.

The diffusion coefficients were fitted using the Arrhenius-type equation:

$$D(T) = D_0 \cdot e^{-\Delta E/k_b T} \tag{12}$$

and the obtained values are reported and compared to the literature data in Table 6. A very good agreement between the calculations of this work and the data from literature can be observed. For oxygen, both D_x and D_z agree well with the previous calculated values of Kulkova *et al.* [31]. Indeed, the high anisotropy for oxygen diffusion between the two crystallographic directions was here confirmed.

For boron, the fit of the tracer diffusion experimental data proposed by Divinski *et al.*[50] leads to a pre-factor $D_0 = 2.48 \pm 2 \cdot 10^{-5}$ m^{2}s^{-1} and an energy barrier $\Delta E = 2.07 \pm 0.17$ eV. The agreement between the measurements

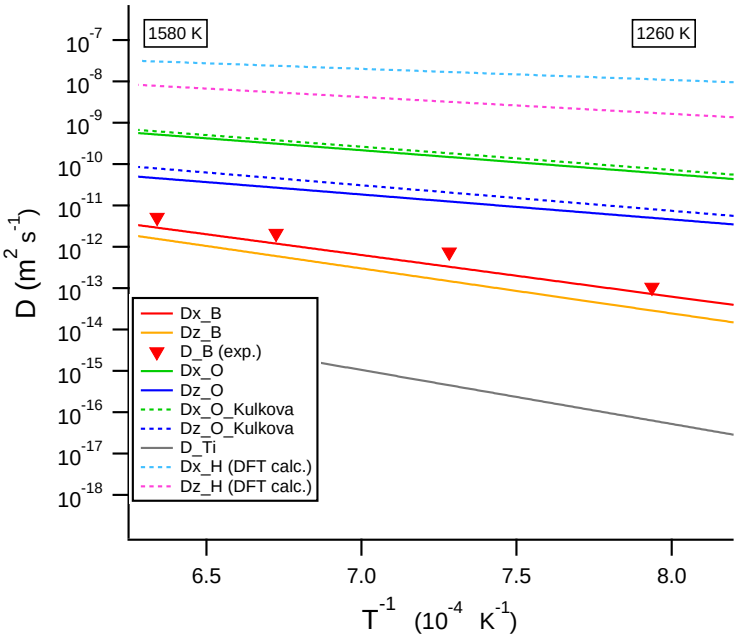

Figure 10: Diffusion coefficients of oxygen (green, blue solid lines) and boron (orange, red solid lines) in γ-TiAl. The calculated curves are compared to: (triangles) the experimental data for boron tracer diffusion [50], (dotted green and blue lines) the calculated values for oxygen by Kulkova [31], (grey line) the titanium self-diffusion [21], (pink, light blue dashed lines) the H diffusion coefficients [40].

Table 6: Activation energy and pre-factor for the diffusion coefficients of oxygen and boron. Experimental values from [50] were obtained on polycristalline samples and hence an effective diffusion coefficient was provided (no distinction between the crystallographic axis).

	Oxygen		Boron	
	This work	Calculated [31]	This work	Experiment [50]
D_0(xy) (m^{2}s^{-1})	$3.5 \cdot 10^{-6}$	$2.3 \cdot 10^{-6}$	$8.1 \cdot 10^{-6}$	$2.48 \pm 2 \cdot 10^{-5}$
D_0(z) (m^{2}s^{-1})	$3.4 \cdot 10^{-7}$	$6.5 \cdot 10^{-7}$	$1.2 \cdot 10^{-5}$	
ΔE(xy) (eV)	1.18	1.11	2.01	2.07 ± 0.17
ΔE(z) (eV)	1.21	1.23	2.15	

and the computations is hence very good, within the experimental uncertainties, especially for the energy barrier. The computed values are indeed only slightly lower than the experimental points. This small difference can be due to the stoichiometry of the alloy experimentally investigated: this was richer in Al (54%) and, as the previous NEB results showed, boron has a higher mobility among the Al-rich interstitial sites, which can explain a slight higher diffusion coefficient.
The diffusion coefficients of boron and oxygen are both much higher than the self-diffusion coefficient of titanium. This is a typical effect of the diffusion mechanism via interstitial sites, which is characteristic of light atoms such as oxygen and boron, while titanium mostly diffuses via vacancies in the lattice. The oxygen diffusion coefficient is higher than that of boron. However, for both these species, the computed values are much lower than the diffusion coefficients reported for hydrogen [40], as one would expect from the difference of mass.

4. Discussion

The solubility of boron and oxygen in the interstitial position of γ-TiAl alloys has been investigated by density functional theory. Three main interstitial sites were investigated at first: two octahedra and one tetrahedron. For both the species, the tetrahedral site has a positive energy of formation, higher than 1 eV (1.678 and 1.350 eV, for boron and oxygen, respectively), indicating that the accommodation in this position is not energetically favoured. For this reason, the tetrahedral sites were neglected in this work.

After checking the dynamic stability, it has been confirmed that boron is accommodated at the centre of the two octahedra present in the lattice, $[Ti_2Al_4]$ and $[Ti_4Al_2]$. The latter is the stablest position for boron, with a negative defect energy of formation. The preference for the Ti-rich site is also consistent with the experimental evidences, which show a precipitation of TiB_2 particles when Ti-Al alloys are doped with boron.

Contrary to boron, the phonon calculations show that oxygen is not really stable in the centres of the two octahedral sites. Applying a small displacement from the centres in order to break symmetry and performing a DFT relaxation of the structures, it has been found out that oxygen occupies two slightly different sites, here named α and β. The first is at the centre of the Al-Al corner in the $[Ti_2Al_4]$ octahedron and it corresponds to a non-regular octahedron, with 2 (closest) Al atoms four Ti atoms at the vertices; the β site is obtained by a small shift along the z direction, toward the top or the bottom, of the $[Ti_4Al_2]$ octahedron centre. This latter, which is still the Ti-richer site, is the one with the lowest energy, in agreement with previous works [26, 27, 28, 29, 31].

The shift from the $[Ti_4Al_2]$ toward β is small and hence the energy difference between the two positions is also limited ($\simeq$ 0.002 eV/atom). On the contrary, the shift from the $[Ti_2Al_4]$ to the α site is not negligible and this result can be surprising, since it has not been reported in the literature before. For instance, Kulkova *et al.* [31], studying the diffusion of oxygen in bulk γ-TiAl, considered the centres of the two octahedra as accommodation sites. However, no phonon calculations were reported in that work to check the dynamic stability and the α sites were not tested. Furthermore, in a previous work from Kulkova *et al.* [29], a similar result was obtained, even if related to surface and not bulk. In [29], the adsorption of oxygen on TiAl(001) surface made of Al atoms was studied and two different accommodation sites were compared: the hollow (H) in the centre of square of surface atoms and bridges sites (B) between Al atoms. These H and B sites correspond to the centre and to the edge of a Al-rich half-octahedron, respectively, and they can hence be compared to the $[Ti_2Al_4]$ and α positions of the bulk. In [29], similarly to the results of these works, it was found that the oxygen is stabler in the bridge site rather than in the hollow.

Once identified the stable interstitial sites, the diffusion of oxygen and boron in γ-TiAl has been investigated by combining NEB and phonon band structure calculations, in the frame of the Transitional State Theory [33]. Since both oxygen and boron can walk various diffusion paths, among the two kinds of interstitial sites identified for each species, the Multi-State Diffusion Method [34] has been adopted to compute the diffusion coefficients in the crystallographic directions. The diffusion was here considered as a regular random walk. Moreover, some approximations were clearly introduced in the method here applied. First, the infinite dilution hypothesis was here adopted. Indeed, the NEB calculations were performed with one single interstitial atom per supercell, implying that defect-defect interactions are neglected. This approximation is reasonable for the specific case: both oxygen and boron have very low solubility in γ-TiAl, hence high concentration of defects would lead to the precipitation of different phases. Second, quantum tunnelling through the energy barriers has not been taken into account. It has been proven that this is important for the diffusion of hydrogen in solid crystals [54], but it is surely negligible for heavier atoms such as boron and oxygen. Finally, the thermal expansion has been neglected, since barrier energies and frequencies were computed for the lattice

parameter obtained for T = 0 K. Nevertheless, the validity of the computation scheme here applied is proved by the good agreement between the calculation results and the experimental data available for boron [50]. The computed activation energies, equal to 2.01 eV (*xy* direction) and 2.15 eV (*z* direction), are in very good agreement with the experimental value determined at 2.07±0.17 eV [50] for a polycristalline material. The calculated prefactor terms are slightly smaller than the experimental one and, as a result, the computed diffusion coefficients are lower than the experimental data (Fig. 10). This small gap is likely due to the differences between the experimental conditions and the computation. The latter were performed simulating an equimolar alloy, while the tracer diffusion measurements were performed on polycrystalline γ-TiAl(54 at.%) samples. The enrichment in aluminium can explain the slightly higher experimental diffusion coefficient. Indeed, the calculations of this work showed that the Al-rich interstitial site are less stable than the Ti-rich positions and they are hence characterized by lower energy barriers, enhancing the diffusion. Moreover, since the polycrystalline samples were used in the experiment, the diffusion could also be enhanced through grain boundaries.

The diffusion coefficients obtained for oxygen are approximately two orders of magnitude higher than that of boron. The values are in good agreement with the previous ones reported by Kulkova *et al.* [31], despite the differences between the two applied computation schemes. These can be summarized in three points: 1) Kulkova *et al.* considered as stable sites the centres of the octahedra [31], while here it was shown that oxygen moves from these positions toward the α and β sites; 2) in [31], the tetrahedral sites were included in the diffusion paths, while they were here neglected; 3) in [31], the prefactor of the diffusion coefficients was approximated as $\sqrt{\Delta E/(2md^2)}$, while here it was obtained from all the vibrational modes (oxygen and lattice atoms), according to the TST. The good agreement between the results indicate that these differences do not affect significantly the diffusion coefficients. As already discussed, the $[Ti_4Al_2]$ and β positions are very close and the energy difference between the two is negligible. The lowering in energy was more significant for the oxygen moving from the $[Ti_2Al_4]$ to the α interstitial site (-0.838 eV for the 333 supercell). The activation energy for the diffusion in the *xy* plane reported by Kulkova *et al.* [31], equal to 1.11 eV, is slightly lower than the one here obtained, equal to 1.18 eV. This difference could be due to the fact that these authors are not considering the stablest position for oxygen in the Al plane, and hence the corresponding barrier energy results lower. However, this difference is very small. Concerning the tetrahedral sites, the good agreement between the two works confirm that these sites do not give a significant contribution to the diffusion. Finally, also the approximation adopted by Kulkova *et al.* [31] for the prefactor ν^* seems valid.

5. Conclusions and perspectives

Ti-Al alloys are suitable materials for the turbomachines in aerospace application. Nowadays, in order to reduce the environmental impact of aeronautical engines, their working temperatures are being increased and the behaviour of these materials in the new conditions needs to be investigated. One crucial aspect is the oxidation resistance of the alloys. Thermodynamic and kinetic databases, based on the CALPHAD approach [66], can be very helpful to predict the life duration of materials in harsh conditions. However, if thermodynamic databases of Ti-Al alloys are currently quite well established [49], kinetic databases are still limited because of the lack of fundamental data, such as diffusion coefficients. In this work, it has been shown that diffusion coefficients of solute atoms in Ti-Al alloys, such as boron and oxygen in the γ-TiAl phase, can be accessed from *ab initio* computations. NEB calculations based on DFT can provide the barrier energy to overcome for the atom jumps among neighbour sites. Attempt frequencies, which are the prefactor terms in the Arrhenius-type equations, are related to the phonon band structures of the lattice. Finally, in case of complex lattices where several diffusion paths are possible, the analytical Multi-state Diffusion Method allows solving the diffusion equation. This computation method has proven to be valid for the system under consideration by the good agreement between the computational results and the experimental data available for boron diffusion in γ-TiAl [50]. Besides, these calculations can easily show anisotropic effects in diffusion, which cannot always be experimentally observed (availability of single crystals). Indeed, for both oxygen and boron in γ-TiAl, the diffusion coefficients in the basal plane ($D_x = D_y$) are higher than in the z direction. For boron, this difference is limited to a factor lower than 2, while the anisotropy is more significant for the oxygen diffusion, with $D_{x,y}$ almost 50 times higher than D_z. These data will be used as input for kinetic database, which is currently under development at the ONERA (the Franch Aerospace Lab).

Appendix A. Effect of the supercell size

The effect of the supercell size on the formation energy of the defects has been estimated by performing calculation on 3x3x3 and 4x4x4 cells. The defects were inserted in the centres of the octahedra sites of the supercells, without relaxing the structures, i.e. keeping cell volumes and atoms positions fixed. The results are shown in table A.7. The difference in energy between the 333 and 444 calculations is very small, always lower than 0.03 eV/atom.

Table A.7: Energies obtained for calculations on 3x3x3 and 4x4x4 supercells.

Defect	333 E_{tot} (eV)	333 E/atom (eV/at.)	444 E_{tot} (eV)	444 E/atom (eV/at.)	ΔE (eV/atom)
O in Ti_2Al_4	-675.0126	-6.1928	-1595.8173	-6.2094	0.017
O in Ti_4Al_2	-675.5622	-6.1978	-1596.8230	-6.2133	0.016
B in Ti_2Al_4	-667.9657	-6.1281	-1582.2319	-6.1565	0.028
B in Ti_4Al_2	-669.0925	-6.1385	-1583.1443	-6.1601	0.022

Appendix B. Transition states

Table B.8: Negative frequencies obtained for the transitional states (highest energy points) of the diffusion paths.

Atom	Path	Negative frequency (THz)
B	Ti_2Al_4-Ti_2Al_4	-3.9
	Ti_4Al_2-Ti_4Al_2	-10.7; -6.7
	Ti_4Al_2-Ti_2Al_4	-6.1
O	α-α	-11.0; -8.0
	β-β	-1.0
	α-β	-5.0

Appendix C. Multi-state model

The expressions of the diffusion coefficients along the different crystallographic directions were obtained from the multi-state diffusion method proposed by Landaman [34, 56]. Here, we explicitly show how the Laplace transform of the waiting time density matrix, $\underline{\psi}(u)$, and the Fourier transform of the displacement matrix, $\underline{p}(\overrightarrow{k})$, were built for boron and oxygen.

Boron. The first step consists in identifying a unit cell and the number of interstitial sites present in it. For the boron case, the unit cell is shown in Fig. C.11, where aluminium and titanium are represented in blue and red, respectively, the Ti_4Al_2 sites are in green and the Ti_2Al_4 are in yellow. There are two Ti_4Al_2 and two Ti_2Al_4 sites per unit cell. An atom in Ti_4Al_2 can jump toward 4 neighbour Ti_4Al_2 sites and eight neighbour Ti_2Al_4 sites. Equivalently, an atom in Ti_2Al_4 can jump toward 4 sites of the same type and 8 Ti_4Al_2 sites. In the following, for simplicity, the octahedral site will be identified only with the most abundant atom (Ti_4Al_2 = Ti4 and Ti_2Al_4 = Al4).

The Laplace transform of the waiting time density matrix $\underline{\psi}(u)$ is given by:

$\underline{\psi}(u) =$

$$
\begin{array}{c} \\ Al_{4_1} \\ Al_{4_2} \\ Ti_{4_1} \\ Ti_{4_2} \end{array}
\begin{array}{c}
\begin{array}{cccc} Al_{4_1} & Al_{4_2} & Ti_{4_1} & Ti_{4_2} \end{array} \\
\begin{pmatrix}
0 & \frac{4\nu_{Al4Al4}}{K_{Al4}(u)} & \frac{4\nu_{Ti4Al4}}{K_{Ti4}(u)} & \frac{4\nu_{Ti4Al4}}{K_{Ti4}(u)} \\
\frac{4\nu_{Al4Al4}}{K_{Al4}(u)} & 0 & \frac{4\nu_{Ti4Al4}}{K_{Ti4}(u)} & \frac{4\nu_{Ti4Al4}}{K_{Ti4}(u)} \\
\frac{4\nu_{Al4Ti4}}{K_{Al4}(u)} & \frac{4\nu_{Al4-Ti4}}{K_{Al4}(u)} & 0 & \frac{4\nu_{Ti4Ti4}}{K_{Ti4}(u)} \\
\frac{4\nu_{Al4Ti4}}{K_{Al4}(u)} & \frac{4\nu_{Al4Ti4}}{K_{Al4}(u)} & \frac{4\nu_{Ti4Ti4}}{K_{Ti4}(u)} & 0
\end{pmatrix}
\end{array}
\tag{C.1}
$$

where ν_{jk} is the jumping rate from site j to site k and

$$K_{Al4}(u) = 4\nu_{Al4Al4} + 8\nu_{Al4Ti4} + u; \tag{C.2}$$

$$K_{Ti4}(u) = 4\nu_{Ti4Ti4} + 8\nu_{Ti4Al4} + u. \tag{C.3}$$

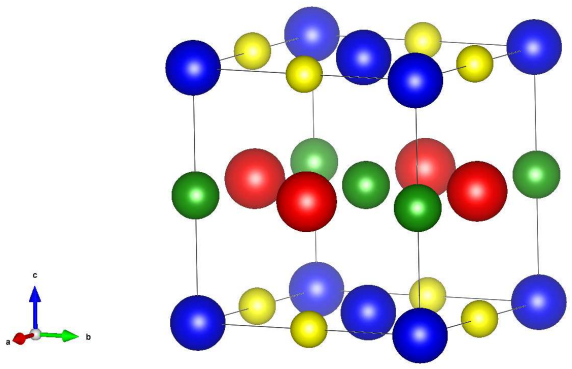

Figure C.11: Cell with [Ti_2Al_4] (yellow) and [Ti_4Al_2] (green) defects. Ti and Al are respectively in red and blue.

For each jump, one needs to specify if the atom leaves or not the cell. The vector $\vec{l_k} - \vec{l_j} = m_1\vec{l_1} + m_2\vec{l_2} + m_3\vec{l_3}$ represents the displacement of an atom jumping from site j to k. The element $p_{jk}(\vec{k})$ of the $\underline{p}(\vec{k})$ matrix is

$$p_{jk}(\vec{k}) = \frac{\sum_{h=1}^{N_{jk}} \delta_{jk}^h}{N_{jk}} \tag{C.4}$$

where the sum is over all the considered paths from a site j to a site k and

$$\delta_{jk}^h = e^{i(m_k^1 l_1 \vec{k_1} + m_k^2 l_2 \vec{k_2} + m_k^3 l_3 \vec{k_3})} \tag{C.5}$$

where m_k values can be equal to 0 or ± 1, depending if the site k is in the same cell or in another one and, in that case, in which direction the cell is repeated. For example, considering an atom in a β site, this can jump to the other β site of the same cell or to 4 different α sites, all belonging to the repeated cell along $\vec{k_3}$. The Fourier transform matrix of the displacement is then:

$$
\underline{p}(\vec{k}) = \begin{array}{c}
\begin{array}{cccc} Al_{4_1} & Al_{4_2} & Ti_{4_1} & Ti_{4_2} \end{array} \\
\begin{pmatrix}
0 & A & B & C \\
D & 0 & E & F \\
G & H & 0 & I \\
L & M & N & 0
\end{pmatrix}
\end{array}
\begin{array}{l} Al_{4_1} \\ Al_{4_2} \\ Ti_{4_1} \\ Ti_{4_2} \end{array}
\tag{C.6}
$$

where

$$A = \frac{1 + e^{i(\frac{a}{2}\vec{k_1} + \frac{a}{2}\vec{k_2})} + e^{i(-\frac{a}{2}\vec{k_1} + \frac{a}{2}\vec{k_2})} + e^{i(-\frac{a}{2}\vec{k_1} - \frac{a}{2}\vec{k_2})}}{4}; \tag{C.7}$$

$$B = \frac{1 + e^{i(\frac{a}{2}\vec{k_1} + \frac{c}{2}\vec{k_3})} + e^{i(-\frac{a}{2}\vec{k_1} + \frac{c}{2}\vec{k_3})} + e^{i(-\frac{a}{2}\vec{k_1} - \frac{c}{2}\vec{k_3})}}{4}; \tag{C.8}$$

$$C = \frac{1 + e^{i(-\frac{a}{2}\vec{k_2} + \frac{c}{2}\vec{k_3})} + e^{i(\frac{a}{2}\vec{k_2} + \frac{c}{2}\vec{k_3})} + e^{i(\frac{a}{2}\vec{k_2} - \frac{c}{2}\vec{k_3})}}{4}; \tag{C.9}$$

$$D = \frac{1 + e^{i(\frac{a}{2}\vec{k_1} + \frac{a}{2}\vec{k_2})} + e^{i(\frac{a}{2}\vec{k_1} - \frac{a}{2}\vec{k_2})} + e^{i(-\frac{a}{2}\vec{k_1} - \frac{a}{2}\vec{k_2})}}{4}; \tag{C.10}$$

$$E = \frac{1 + e^{i(\frac{a}{2}\vec{k_2} + \frac{c}{2}\vec{k_3})} + e^{i(-\frac{a}{2}\vec{k_2} + \frac{c}{2}\vec{k_3})} + e^{i(-\frac{a}{2}\vec{k_2} - \frac{c}{2}\vec{k_3})}}{4}; \tag{C.11}$$

$$F = \frac{1 + e^{i(\frac{a}{2}\vec{k_1} - \frac{c}{2}\vec{k_3})} + e^{i(\frac{a}{2}\vec{k_1} + \frac{c}{2}\vec{k_3})} + e^{i(-\frac{a}{2}\vec{k_1} + \frac{c}{2}\vec{k_3})}}{4}; \tag{C.12}$$

$$G = \frac{1 + e^{i(-\frac{a}{2}\vec{k_1} - \frac{c}{2}\vec{k_3})} + e^{i(\frac{a}{2}\vec{k_1} - \frac{c}{2}\vec{k_3})} + e^{i(\frac{a}{2}\vec{k_1} + \frac{c}{2}\vec{k_3})}}{4}; \tag{C.13}$$

$$H = \frac{1 + e^{i(\frac{a}{2}\vec{k_2} + \frac{c}{2}\vec{k_3})} + e^{i(\frac{a}{2}\vec{k_2} - \frac{c}{2}\vec{k_3})} + e^{i(-\frac{a}{2}\vec{k_2} - \frac{c}{2}\vec{k_3})}}{4}; \tag{C.14}$$

$$I = \frac{1 + e^{i(-\frac{a}{2}\vec{k_1} + \frac{a}{2}\vec{k_2})} + e^{i(\frac{a}{2}\vec{k_1} + \frac{a}{2}\vec{k_2})} + e^{i(+\frac{a}{2}\vec{k_1} - \frac{a}{2}\vec{k_2})}}{4}; \tag{C.15}$$

$$L = \frac{1 + e^{i(\frac{a}{2}\vec{k_2} - \frac{c}{2}\vec{k_3})} + e^{i(-\frac{a}{2}\vec{k_2} - \frac{c}{2}\vec{k_3})} + e^{i(-\frac{a}{2}\vec{k_2} + \frac{c}{2}\vec{k_3})}}{4}; \tag{C.16}$$

$$M = \frac{1 + e^{i(-\frac{a}{2}\vec{k_1} + \frac{c}{2}\vec{k_3})} + e^{i(-\frac{a}{2}\vec{k_1} - \frac{c}{2}\vec{k_3})} + e^{i(\frac{a}{2}\vec{k_1} - \frac{c}{2}\vec{k_3})}}{4}; \tag{C.17}$$

$$N = \frac{1 + e^{i(\frac{a}{2}\vec{k_1} - \frac{a}{2}\vec{k_2})} + e^{i(-\frac{a}{2}\vec{k_1} - \frac{a}{2}\vec{k_2})} + e^{i(-\frac{a}{2}\vec{k_1} + \frac{a}{2}\vec{k_2})}}{4}; \tag{C.18}$$

The propagator matrix $\underline{R}(\vec{k}, u)$ is then find using Eq. 5 and the diffusion coefficient is obtained by Eq. 6-8. For boron, it was obtained:

$$D_{x,y} = \frac{11a^2(\nu_{Al4Al4}\nu_{Ti4Al4} + \nu_{Al4Ti4}(2\nu_{Ti4Al4} + \nu_{Ti4Ti4}))}{32(\nu_{Al4Ti4} + \nu_{Ti4Al4})} \tag{C.19}$$

$$D_z = \frac{11c^2\nu_{Al4Ti4}\nu_{Ti4Al4}}{8(\nu_{Al4Ti4} + \nu_{Ti4Al4})} \tag{C.20}$$

Oxygen. For the oxygen, the distortion of the octahedral sites in the α and β sites leads to a more complex unit cell, as the one shown in Fig. C.12. In this case, there are four α and four β interstitial sites per unite cell. An atom in the α site can jumps to other 4 α sites (moving along the a or b direction) and to 4 β sites. An atom in a β site can jump toward 4 α site, but only toward one other β site, the closest one in the c direction. Indeed, the NEB calculations showed that diffusion toward the other β sites occurs passing first through the α ones.

The relative Laplace transform of the waiting time density matrix $\underline{\phi}(u)$ is:

$\underline{\psi}(u) =$

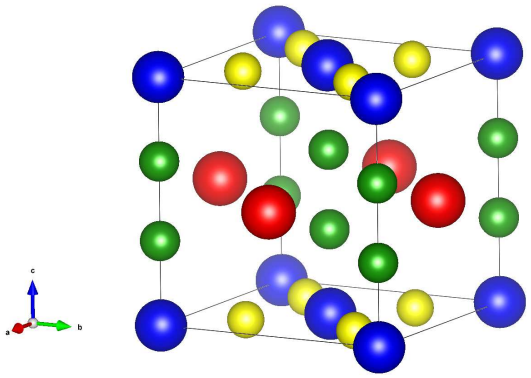

Figure C.12: Cell with α (yellow) and β (green) defects. Ti and Al are respectively in red and blue.

$$
\begin{array}{c}
 \\ \alpha_1 \\ \alpha_2 \\ \alpha_3 \\ \alpha_4 \\ \beta_1 \\ \beta_2 \\ \beta_3 \\ \beta_4
\end{array}
\begin{array}{c}
\begin{array}{cccccccc} \alpha_1 & \alpha_2 & \alpha_3 & \alpha_4 & \beta_1 & \beta_2 & \beta_3 & \beta_4 \end{array} \\
\begin{pmatrix}
0 & \frac{2\nu_{\alpha\alpha}}{K_\alpha} & 0 & \frac{2\nu_{\alpha\alpha}}{K_\alpha} & \frac{\nu_{\beta\alpha}}{K_\beta} & \frac{\nu_{\beta\alpha}}{K_\beta} & \frac{\nu_{\beta\alpha}}{K_\beta} & \frac{\nu_{\beta\alpha}}{K_\beta} \\
\frac{2\nu_{\alpha\alpha}}{K_\alpha} & 0 & \frac{2\nu_{\alpha\alpha}}{K_\alpha} & 0 & \frac{\nu_{\beta\alpha}}{K_\beta} & \frac{\nu_{\beta\alpha}}{K_\beta} & \frac{\nu_{\beta\alpha}}{K_\beta} & \frac{\nu_{\beta\alpha}}{K_\beta} \\
0 & \frac{2\nu_{\alpha\alpha}}{K_\alpha} & 0 & \frac{2\nu_{\alpha\alpha}}{K_\alpha} & \frac{\nu_{\beta\alpha}}{K_\beta} & \frac{\nu_{\beta\alpha}}{K_\beta} & \frac{\nu_{\beta\alpha}}{K_\beta} & \frac{\nu_{\beta\alpha}}{K_\beta} \\
\frac{2\nu_{\alpha\alpha}}{K_\alpha} & 0 & \frac{2\nu_{\alpha\alpha}}{K_\alpha} & 0 & \frac{\nu_{\beta\alpha}}{K_\beta} & \frac{\nu_{\beta\alpha}}{K_\beta} & \frac{\nu_{\beta\alpha}}{K_\beta} & \frac{\nu_{\beta\alpha}}{K_\beta} \\
\frac{\nu_{\alpha\beta}}{K_\alpha} & \frac{\nu_{\alpha\beta}}{K_\alpha} & \frac{\nu_{\alpha\beta}}{K_\alpha} & \frac{\nu_{\alpha\beta}}{K_\alpha} & 0 & \frac{\nu_{\beta\beta}}{K_\beta} & 0 & 0 \\
\frac{\nu_{\alpha\beta}}{K_\alpha} & \frac{\nu_{\alpha\beta}}{K_\alpha} & \frac{\nu_{\alpha\beta}}{K_\alpha} & \frac{\nu_{\alpha\beta}}{K_\alpha} & \frac{\nu_{\beta\beta}}{K_\beta} & 0 & 0 & 0 \\
\frac{\nu_{\alpha\beta}}{K_\alpha} & \frac{\nu_{\alpha\beta}}{K_\alpha} & \frac{\nu_{\alpha\beta}}{K_\alpha} & \frac{\nu_{\alpha\beta}}{K_\alpha} & 0 & 0 & 0 & \frac{\nu_{\beta\beta}}{K_\beta} \\
\frac{\nu_{\alpha\beta}}{K_\alpha} & \frac{\nu_{\alpha\beta}}{K_\alpha} & \frac{\nu_{\alpha\beta}}{K_\alpha} & \frac{\nu_{\alpha\beta}}{K_\alpha} & 0 & 0 & \frac{\nu_{\beta\beta}}{K_\beta} & 0
\end{pmatrix}
\end{array}
\tag{C.21}
$$

With

$$K_\alpha = 4\nu_{\alpha\alpha} + 4\nu_{\alpha\beta} + u; \tag{C.22}$$

$$K_\beta = \nu_{\beta\beta} + 4\nu_{\beta\alpha} + u; \tag{C.23}$$

The Fourier transform matrix of the displacement is:

$$
\begin{array}{c}
 \\ \alpha_1 \\ \alpha_2 \\ \alpha_3 \\ \alpha_4 \\ \beta_1 \\ \beta_2 \\ \beta_3 \\ \beta_4
\end{array}
\begin{array}{c}
\begin{array}{cccccccc} \alpha_1 & \alpha_2 & \alpha_3 & \alpha_4 & \beta_1 & \beta_2 & \beta_3 & \beta_4 \end{array} \\
\begin{pmatrix}
0 & A & 0 & B & 1 & C & 1 & D \\
Aa & 0 & B & 0 & H & G & 1 & Ee \\
0 & Bb & 0 & Aa & Ii & D & 1 & C \\
Bb & 0 & A & 0 & L & Ee & 1 & G \\
1 & Ee & C & G & 0 & 1 & 0 & 0 \\
Ii & L & M & H & 1 & 0 & 0 & 0 \\
1 & 1 & 1 & 1 & 0 & 0 & 0 & 1 \\
M & H & Ii & L & 0 & 0 & 1 & 0
\end{pmatrix}
\end{array}
\tag{C.24}
$$

$$A = \frac{1 + e^{i\frac{a}{2}\overrightarrow{k_1}}}{2}; \tag{C.25}$$

$$B = \frac{1 + e^{i\frac{a}{2}\overrightarrow{k_2}}}{2}; \tag{C.26}$$

$$Aa = \frac{1 + e^{-i\frac{a}{2}\overrightarrow{k_1}}}{2}; \tag{C.27}$$

$$Bb = \frac{1 + e^{-i\frac{a}{2}\overrightarrow{k_2}}}{2}; \tag{C.28}$$

$$Cc = e^{i(\frac{a}{4}\overrightarrow{k_1} + \frac{a}{4}\overrightarrow{k_2} + \frac{c}{3}\overrightarrow{k_3})}; \tag{C.29}$$

$$D = e^{i(-\frac{a}{4}\overrightarrow{k_1} - \frac{a}{4}\overrightarrow{k_2} + \frac{c}{3}\overrightarrow{k_3})}; \tag{C.30}$$

$$E = e^{i(\frac{a}{4}\overrightarrow{k_1} - \frac{a}{4}\overrightarrow{k_2} + \frac{c}{3}\overrightarrow{k_3})}; \tag{C.31}$$

$$G = e^{i(-\frac{a}{4}\overrightarrow{k_1} + \frac{a}{4}\overrightarrow{k_2} + \frac{c}{3}\overrightarrow{k_3})}; \tag{C.32}$$

$$H = e^{i(-\frac{a}{4}\overrightarrow{k_1} + \frac{a}{4}\overrightarrow{k_2} - \frac{c}{3}\overrightarrow{k_3})}; \tag{C.33}$$

$$Ii = e^{i(-\frac{a}{4}\overrightarrow{k_1} - \frac{a}{4}\overrightarrow{k_2} - \frac{c}{3}\overrightarrow{k_3})}; \tag{C.34}$$

$$L = e^{i(\frac{a}{4}\overrightarrow{k_1} - \frac{a}{4}\overrightarrow{k_2} - \frac{c}{3}\overrightarrow{k_3})}; \tag{C.35}$$

$$M = e^{i(\frac{a}{4}\overrightarrow{k_1} + \frac{a}{4}\overrightarrow{k_2} - \frac{c}{3}\overrightarrow{k_3})}; \tag{C.36}$$

The propagator matrix $\underline{R}(\overrightarrow{k}, u)$ is then find using Eq. 5 and the diffusion coefficient is obtained by Eq. 6-8.

Data availability Statements

Further data can be provided on requirements.

Acknowledgements

Authors are grateful to doctor Daniele Sciannandrone for useful discussions.

References

[1] F. H. Froes, C. Suryanarayana, D. Eliezer, Synthesis, properties and applications of titanium aluminides, Journal of Materials Science 27 (19) (1992) 5113–5140. doi:10.1007/BF02403806.
URL https://doi.org/10.1007/BF02403806

[2] F. Appel, R. Wagner, Microstructure and deformation of two-phase gamma-titanium aluminides, Materials Science and Engineering: R: Reports 22 (5) (1998) 187–268. doi:10.1016/S0927-796X(97)00018-1.
URL http://www.sciencedirect.com/science/article/pii/S0927796X97000181

[3] M. Perrut, P. Caron, M. Thomas, A. Couret, High temperature materials for aerospace applications: Ni-based superalloys and gamma-TiAl alloys, Comptes Rendus Physique 19 (8) 657–671. doi:10.1016/j.crhy.2018.10.002.

[4] V. T. Witusiewicz, B. Hallstedt, A. A. Bondar, U. Hecht, S. V. Sleptsov, T. Y. Velikanova, Thermodynamic description of the Al–C–Ti system, Journal of Alloys and Compounds 623 480–496. doi:10.1016/j.jallcom.2014.10.119.

[5] Y. Umakoshi, M. Yamaguchi, T. Sakagami, T. Yamane, Oxidation resistance of intermetallic compounds Al3ti and TiAl, Journal of Materials Science 24 (5) (1989) 1599–1603. doi:10.1007/BF01105677.
URL https://doi.org/10.1007/BF01105677

[6] S. Becker, A. Rahmel, M. Schorr, M. Schütze, Mechanism of isothermal oxidation of the intermetallic TiAl and of TiAl alloys, Oxidation of Metals 38 (5) (1992) 425–464. doi:10.1007/BF00665663.
URL https://doi.org/10.1007/BF00665663

[7] C. Lang, M. Schütze, TEM investigations of the early stages of TiAl oxidation, Oxidation of Metals 46 (3) (1996) 255–285. doi:10.1007/BF01050799.
URL https://doi.org/10.1007/BF01050799

[8] M. Schmitz-Niederau, M. Schutze, The Oxidation Behavior of Several Ti-Al Alloys at 900 C in Air, Oxidation of Metals 52 (3) (1999) 225–240. doi:10.1023/A:1018839511102.
URL https://doi.org/10.1023/A:1018839511102

[9] V. Shemet, A. Tyagi, J. Becker, P. Lersch, L. Singheiser, W. Quadakkers, Formation of protective alumina-based scales during high-temperature air oxidation of γ-TiAl alloys, Oxidation of Metals 54 (3) (2000) 211–235, cited By 57.
URL http://www.scopus.com/inward/record.url?eid=2-s2.0-0034300689&partnerID=40&md5=0d5b59b686dd9605b680b912e5082f01

[10] V. Shemet, A. Tyagi, J. Penkalla, L. Singheiser, J. Becker, W. Quadakkers, Mechanisms of scale formation on new alumina forming γ-TiAl alloys studied by MCs+-SIMS, Materials at High Temperatures 17 (1) (2000) 41–47, cited By 10.
URL http://www.scopus.com/inward/record.url?eid=2-s2.0-0002054490&partnerID=40&md5=8e7c3e55e885e4ebf6e30047254e1052

[11] L. Teng, D. Nakatomi, S. Seetharaman, Oxidation Behavior of TiAl-8Nb Turbine Blade Alloy, Metallurgical and Materials Transactions B 38 (3) (2007) 477–484. doi:10.1007/s11663-007-9061-2.
URL https://doi.org/10.1007/s11663-007-9061-2

[12] H. Kawaura, H. Kawahara, K. Nishino, T. Saito, New surface treatment using shot blast for improving oxidation resistance of TiAl-base alloys, Materials Science and Engineering: A 329-331 (2002) 589 – 595. doi:https://doi.org/10.1016/S0921-5093(01)01585-4.
URL http://www.sciencedirect.com/science/article/pii/S0921509301015854

[13] H. Jiang, M. Hirohasi, Y. Lu, H. Imanari, Effect of Nb on the high temperature oxidation of Ti–(0–50 at.%)Al, Scripta Materialia 46 (9) (2002) 639 – 643. doi:https://doi.org/10.1016/S1359-6462(02)00042-8.
URL http://www.sciencedirect.com/science/article/pii/S1359646202000428

[14] S. K. Varma, A. Chan, B. N. Mahapatra, Static and Cyclic Oxidation of Ti–44Al and Ti–44Al–xNb Alloys, Oxidation of Metals 55 (5) (2001) 423–435. doi:10.1023/A:1010351613733.

[15] M. Schütze, M. Hald, Improvement of the oxidation resistance of TiAl alloys by using the chlorine effect, Materials Science and Engineering: A 239-240 (1997) 847 – 858, 4th Conference on High-Temperature Intermetallics. doi:https://doi.org/10.1016/S0921-5093(97)00675-8.

[16] N. Zheng, W. Fischer, H. Grübmeier, V. Shemet, W. Quadakkers, The significance of sub-surface depletion layer composition for the oxidation behaviour of γ-titanium aluminides, Scripta Metallurgica et Materialia 33 (1) (1995) 47 – 53. doi:http://dx.doi.org/10.1016/0956-716X(95)00155-O.

[17] L. Niewolak, V. Shemet, C. Thomas, P. Lersch, L. Singheiser, W. Quadakkers, Oxidation behaviour of Ag-containing TiAl-based intermetallics, Intermetallics 12 (12) (2004) 1387 – 1396. doi:http://dx.doi.org/10.1016/j.intermet.2004.04.040.
URL http://www.sciencedirect.com/science/article/pii/S0966979504001578

[18] J. Małecka, Transformation and precipitation processes in a metal substrate of oxidized TiAl-based alloys, Oxidation of Metals 91 (3) 365–380. doi:10.1007/s11085-019-09886-1.
URL https://doi.org/10.1007/s11085-019-09886-1

[19] C. Herzig, T. Przeorski, Y. Mishin, Self-diffusion in gamma-TiAl: an experimental study and atomistic calculations, Intermetallics 7 (3) 389–404. doi:10.1016/S0966-9795(98)00117-4.
URL http://www.sciencedirect.com/science/article/pii/S0966979598001174

[20] C. Herzig, M. Friesel, D. Derdau, S. V. Divinski, Tracer diffusion behavior of ga as an al-substituting element in ti3al and TiAl intermetallic compounds, Intermetallics 7 (10) 1141–1151. doi:10.1016/S0966-9795(99)00028-X.
URL http://www.sciencedirect.com/science/article/pii/S096697959900028X

[21] Y. Mishin, C. Herzig, Diffusion in the ti–al system, Acta Materialia 48 (3) 589–623. doi:10.1016/S1359-6454(99)00400-0.
URL http://www.sciencedirect.com/science/article/pii/S1359645499004000

[22] Y. Koizumi, M. Kishimoto, Y. Minamino, H. Nakajima, Oxygen diffusion in Ti3al single crystals, Philosophical Magazine 88 (24) (2008) 2991–3010. doi:10.1080/14786430802419135.
URL https://doi.org/10.1080/14786430802419135

[23] A. V. Bakulin, A. M. Latyshev, S. E. Kulkova, Absorption and diffusion of oxygen in the Ti3al alloy, Journal of Experimental and Theoretical Physics 125 (1) (2017) 138–147. doi:10.1134/S1063776117070019.
URL https://doi.org/10.1134/S1063776117070019

[24] H. J. Seifert, A. Kussmaul, F. Aldinger, Phase equilibria and diffusion paths in the ti–al–o–n system, Journal of Alloys and Compounds 317-318 19–25. doi:10.1016/S0925-8388(00)01409-2.
URL http://www.sciencedirect.com/science/article/pii/S0925838800014092

[25] S. Das, The Al-O-Ti (Aluminum-oxygen-titanium) system, Journal of Phase Equilibria 23 (6) (2002) 525–536. doi:10.1361/105497102770331271.
URL https://doi.org/10.1361/105497102770331271

[26] S. W. Hong Li, S. W. Hong Li, Initial Oxidation of gamma-TiAl(111) Surface: Density-functional Theory Study, Journal of Materials Sciences and Technology 25 (04) (2009) 569–576.

[27] S.-Y. Liu, J.-X. Shang, F.-H. Wang, Y. Zhang, Ab initio study of surface self-segregation effect on the adsorption of oxygen on the gamma-TiAl (111) surface, Physical Review B 79 (7) (2009) 075419.

[28] Y. Song, F. J. Xing, J. H. Dai, R. Yang, First-principles study of influence of Ti vacancy and Nb dopant on the bonding of TiAl/TiO2 interface, Intermetallics 49 (2014) 1–6. doi:10.1016/j.intermet.2014.01.001.
URL http://www.sciencedirect.com/science/article/pii/S0966979514000028

[29] S. E. Kulkova, A. V. Bakulin, Q. M. Hu, R. Yang, Adsorption and diffusion of oxygen on gamma-TiAl(001) and (100) surfaces, Computational Materials Science 97 (2015) 55–63. doi:10.1016/j.commatsci.2014.10.007.

URL http://www.sciencedirect.com/science/article/pii/S0927025614006818
[30] C. Y. Zhao, X. Wang, F. H. Wang, First-Principles Study of Nb Doping Effect on the Diffusion of Oxygen Atom in gamma-TiAl (2011). doi:10.4028/www.scientific.net/AMR.304.148.
URL https://www.scientific.net/AMR.304.148
[31] S. E. Kulkova, A. V. Bakulin, S. S. Kulkov, First-Principles Calculations of Oxygen Diffusion in Ti-Al Alloys, Latvian Journal of Physics and Technical Sciences 55 (6) (2018) 20–29. doi:10.2478/lpts-2018-0040.
URL https://content.sciendo.com/view/journals/lpts/55/6/article-p20.xml
[32] Y. A. Bertin, J. Parisot, J. L. Gacougnolle, Modèle atomique de diffusion de l'oxygène dans le titane alpha, Journal of the Less Common Metals 69 (1) (1980) 121–138. doi:10.1016/0022-5088(80)90049-1.
URL http://www.sciencedirect.com/science/article/pii/0022508880900491
[33] H. Eyring, The activated complex in chemical reactions, The Journal of Chemical Physics 3 (2) 107–115. doi:10.1063/1.1749604.
URL https://aip.scitation.org/doi/10.1063/1.1749604
[34] U. Landman, M. F. Shlesinger, Stochastic theory of multistate diffusion in perfect and defective systems. I. mathematical formalism, Physical Review B 19 (12) 6207–6219. doi:10.1103/PhysRevB.19.6207.
URL https://link.aps.org/doi/10.1103/PhysRevB.19.6207
[35] L. Scotti, A. Mottura, Interstitial diffusion of o, n, and c in alpha-ti from first-principles: Analytical model and kinetic monte carlo simulations, The Journal of Chemical Physics 144 (8) 084701. doi:10.1063/1.4942030.
URL https://aip.scitation.org/doi/10.1063/1.4942030
[36] D. Connetable, M. David, Diffusion of interstitial species (h and o atoms) in fcc systems (al, cu, co, ni and pd): Contribution of first and second order transition states, Journal of Alloys and Compounds 772 280–287. doi:10.1016/j.jallcom.2018.09.042.
URL http://www.sciencedirect.com/science/article/pii/S0925838818332717
[37] H. H. Wu, D. R. Trinkle, Direct diffusion through interpenetrating networks: Oxygen in titanium, Physical Review Letters 107 (4). doi:10.1103/PhysRevLett.107.045504.
URL https://link.aps.org/doi/10.1103/PhysRevLett.107.045504
[38] D. Connétable, J. Huez, r. Andrieu, C. Mijoule, , Journal of Physics: Condensed Matter 23 (40) 405401. doi:10.1088/0953-8984/23/40/405401.
URL https://doi.org/10.1088%2F0953-8984%2F23%2F40%2F405401
[39] E. Wimmer, W. Wolf, J. Sticht, P. Saxe, C. B. Geller, R. Najafabadi, G. A. Young, Temperature-dependent diffusion coefficients from ab initio computations: Hydrogen, deuterium, and tritium in nickel, Physical Review B 77 (13) 134305. doi:10.1103/PhysRevB.77.134305.
URL https://link.aps.org/doi/10.1103/PhysRevB.77.134305
[40] D. Connetable, Theoretical study on hydrogen solubility and diffusivity in the gamma-TiAl l10 structure, International Journal of Hydrogen Energy 44 (23) 12215–12227. doi:10.1016/j.ijhydene.2019.03.110.
URL http://www.sciencedirect.com/science/article/pii/S0360319919311176
[41] C. R. Feng, D. J. Michel, C. R. Crowe, The effects of boron in TiAl/ti3al, Scripta Metallurgica 23 (10) 1707–1711. doi:10.1016/0036-9748(89)90347-5.
URL http://www.sciencedirect.com/science/article/pii/0036974889903475
[42] T. Nakano, Y. Umakoshi, Effect of boron addition on the plastic behaviour of polysynthetically twinned crystals of TiAl, Intermetallics 2 (3) 185–191. doi:10.1016/0966-9795(94)90057-4.
URL http://www.sciencedirect.com/science/article/pii/0966979594900574
[43] T. T. Cheng, The mechanism of grain refinement in TiAl alloys by boron addition — an alternative hypothesis, Intermetallics 8 (1) 29–37. doi:10.1016/S0966-9795(99)00063-1.
URL http://www.sciencedirect.com/science/article/pii/S0966979599000631
[44] W. J. Zhang, S. C. Deevi, An analysis of the lamellar transformation in TiAl alloys containing boron, Materials Science and Engineering: A 337 (1) 17–20. doi:10.1016/S0921-5093(02)00017-5.
URL http://www.sciencedirect.com/science/article/pii/S0921509302000175
[45] D. Hu, Effect of boron addition on tensile ductility in lamellar TiAl alloys, Intermetallics 10 (9) 851–858. doi:10.1016/S0966-9795(02)00087-0.
URL http://www.sciencedirect.com/science/article/pii/S0966979502000870
[46] W. D. Wang, Y. C. Ma, B. Chen, M. Gao, K. Liu, Y. Y. Li, Effects of boron addition on grain refinement in TiAl-based alloys, Journal of Materials Science & Technology 26 (7) 639–647. doi:10.1016/S1005-0302(10)60099-0.
URL http://www.sciencedirect.com/science/article/pii/S1005030210600990
[47] A. V. Kartavykh, M. V. Gorshenkov, D. A. Podgorny, Grain refinement mechanism in advanced gamma-TiAl boron-alloyed structural intermetallics: The direct observation, Materials Letters 142 294–298. doi:10.1016/j.matlet.2014.12.025.
URL http://www.sciencedirect.com/science/article/pii/S0167577X14021910
[48] D. J. Larson, C. T. Liu, M. K. Miller, Boron solubility and boride compositions in alpha2 + gamma titanium aluminides, Intermetallics 5 (6) 411–414. doi:10.1016/S0966-9795(97)00016-2.
URL http://www.sciencedirect.com/science/article/pii/S0966979597000162
[49] V. T. Witusiewicz, A. A. Bondar, U. Hecht, J. Zollinger, L. V. Artyukh, T. Y. Velikanova, The al–b–nb–ti system: V. thermodynamic description of the ternary system al–b–ti, Journal of Alloys and Compounds 474 (1) 86–104. doi:10.1016/j.jallcom.2008.06.128.
URL http://www.sciencedirect.com/science/article/pii/S0925838808010438
[50] S. V. Divinski, F. Hisker, T. Wilger, M. Friesel, C. Herzig, Tracer diffusion of boron in alpha-ti and gamma-TiAl, Intermetallics 16 (2) 148–155. doi:10.1016/j.intermet.2007.08.008.
URL http://www.sciencedirect.com/science/article/pii/S0966979507001781
[51] G. Kresse, J. Hafner, *Ab initio* molecular dynamics for liquid metals, Phys. Rev. B 47 (1993) 558–561. doi:10.1103/PhysRevB.47.558.
[52] G. Kresse, J. Furthmüller, Efficient iterative schemes for *ab initio* total-energy calculations using a plane-wave basis set, Phys. Rev. B 54

(1996) 11169–11186. doi:10.1103/PhysRevB.54.11169.
URL http://link.aps.org/doi/10.1103/PhysRevB.54.11169

[53] D. Connétable, M. David, Diffusion of interstitial species (h and o atoms) in fcc systems (al, cu, co, ni and pd): Contribution of first and second order transition states, Journal of Alloys and Compounds 772 280–287. doi:10.1016/j.jallcom.2018.09.042.
URL http://www.sciencedirect.com/science/article/pii/S0925838818332717

[54] P. G. Sundell, M. E. Bjorketun, G. Wahnstrom, Density-functional calculations of prefactors and activation energies for H diffusion in $BaZrO_3$, Physical Review B 76 (9) 094301. doi:10.1103/PhysRevB.76.094301.

[55] C. Wert, C. Zener, Interstitial atomic diffusion coefficients, Physical Review 76 (8) 1169–1175. doi:10.1103/PhysRev.76.1169.

[56] U. Landman, M. F. Shlesinger, Stochastic theory of multistate diffusion in perfect and defective systems. II. case studies, Physical Review B 19 (12) 6220–6237. doi:10.1103/PhysRevB.19.6220.
URL https://link.aps.org/doi/10.1103/PhysRevB.19.6220

[57] D. Watanabé, J. R. Castles, A. Jostsons, A. S. Malin, The ordered structure of TiO, Acta Crystallographica 23 (2) (1967) 307–313. doi:10.1107/S0365110X67002634.
URL http://dx.doi.org/10.1107/S0365110X67002634

[58] G. Kresse, D. Joubert, From ultrasoft pseudopotentials to the projector augmented-wave method, Phys. Rev. B 59 (1999) 1758–1775. doi:10.1103/PhysRevB.59.1758.

[59] J. P. Perdew, K. Burke, M. Ernzerhof, Generalized Gradient Approximation Made Simple [Phys. Rev. Lett. 77, 3865 (1996)], Physical Review Letters 78 (7) (1997) 1396–1396. doi:10.1103/PhysRevLett.78.1396.
URL https://link.aps.org/doi/10.1103/PhysRevLett.78.1396

[60] A. Togo, I. Tanaka, First principles phonon calculations in materials science, Scripta Materialia 108 1–5. doi:10.1016/j.scriptamat.2015.07.021.

[61] W. B. Pearson, Handbook of Lattice Spacing and Structures of Metals and Alloys, Pergamon Press, 1964.

[62] R. Hultgren, P. D. Desai, D. T. Hawkins, M. Gleiser, K. K. Kelley, Selected Values of the Thermodynamic Properties of Binary Alloys, ohio Edition, 1973.

[63] C. Freysoldt, B. Grabowski, T. Hickel, J. Neugebauer, G. Kresse, A. Janotti, C. G. Van de Walle, First-principles calculations for point defects in solids, Rev. Mod. Phys. 86 (2014) 253–305. doi:10.1103/RevModPhys.86.253.
URL http://link.aps.org/doi/10.1103/RevModPhys.86.253

[64] A. Stoliaroff, S. Jobic, C. Latouche, New insights into the determination of maximum chemical potentials to account for alkali doping in beta-In2s3 by ab initio calculations, Computational Materials Science 168 (2019) 221–228. doi:10.1016/j.commatsci.2019.06.011.
URL http://www.sciencedirect.com/science/article/pii/S0927025619303672

[65] J. Stráský, M. Janeček, P. Harcuba, D. Preisler, M. Landa, 4.2 - Biocompatible beta-Ti alloys with enhanced strength due to increased oxygen content, in: F. H. Froes, M. Qian (Eds.), Titanium in Medical and Dental Applications, Woodhead Publishing Series in Biomaterials, Woodhead Publishing, 2018, pp. 371–392. doi:10.1016/B978-0-12-812456-7.00017-2.
URL http://www.sciencedirect.com/science/article/pii/B9780128124567000172

[66] A. Borgenstam, L. Höglund, J. Ågren, A. Engström, DICTRA, a tool for simulation of diffusional transformations in alloys, Journal of Phase Equilibria 21 (3) 269. doi:10.1361/105497100770340057.
URL https://doi.org/10.1361/105497100770340057